INVERSE METHOD TO ESTIMATE HEAT GENERATION RATES IN LITHIUM ION CELLS

A Thesis

by

HANUMANTH REDDY PALLE

Submitted to the Office of Graduate and Professional Studies of
Texas A&M University
in partial fulfillment of the requirements for the degree of

MASTER OF SCIENCE

Chair of Committee,	Partha P. Mukherjee
Committee Members,	Waruna Kulatilaka
	Sarbajit Banerjee
Head of Department,	Daniel McAdams

May 2017

Major Subject: Mechanical Engineering

ABSTRACT

Li-ion batteries represent a pinnacle of compact energy storage. This size reduction makes them very energy dense systems, thus substantially increasing the chances of the mishap. Future applications demand a very good rate capability (i.e., fast charging), which invariably leads to higher heat generation. This heat if not dissipated properly, rapidly increases the cell temperature and eventually leads to thermal runaway. Thus, the knowledge of heat generation as a function of current is of utmost importance for the design of cooling systems. Heat generation rates are most commonly quantified using accelerating rate calorimeter.

In this study, a calorimeter-free method based on inverse heat transfer analysis is proposed. 18650 cells are electrochemically cycled at different currents (C-rate) with consecutive charge-rest-discharge-rest cycles in a constant temperature ambient. During the experiments cell temperature, ambient temperature, current and voltage data is recorded. An energy balance is carried out to model the thermal response of the 18650 cell during electrochemical cycling. The model involves volumetric heat generation rate and convective heat transfer coefficient as unknowns which are characterized by inverse heat transfer analysis. Convective heat transfer coefficient is computed from data during rest periods. It is then used to quantify heat generation rate as a function of charge/discharge capacity and C-rate. At low current operation, the contribution of reversible heat is of the similar order to irreversible heat and would lead to qualitatively different heat generation profiles during charging and discharging. On the other hand, at higher currents, irreversible heat dominates and the heat generation rates during charge and discharge are quite similar, both qualitatively and quantitatively.

The contribution of various sources towards total heat generation has been quantified. Effect of capacity fade on internal resistances and heat generation rates, while cycling at various C-rates, has been investigated. At higher C-rates, the contribution of reversible heat towards the total heat generation is found to be negligible while that of irreversible ohmic heat is found to be major and is closely related to the internal resistance. Internal resistance is found to be independent of C-rate of operation, and increasing with capacity fade in a cell.

DEDICATION

I would like to dedicate this work to my family.

ACKNOWLEDGEMENTS

I would like to thank my committee chair, Dr. Partha P. Mukherjee, and my committee members, Dr. Waruna Kulatilaka, Dr. Sarbajit Banerjee for their guidance and support throughout the course of this research.

Thanks also go to my friends and colleagues and the department faculty and staff for making my time at Texas A&M University a great experience. I would also like to thank my mentors for guiding me through all the ups and downs of my life.

Finally, thanks to my mother, father and sister for their encouragement and love.

CONTRIBUTORS AND FUNDING SOURCES

This work was supervised by a thesis committee consisting of Professor Partha P. Mukherjee and Professor Waruna Kulatilaka of the Department of Mechanical Engineering and Professor Sarbajit Banerjee of the Department of Chemistry.

All work for the thesis was completed by the student, under the advisement of Partha P. Mukherjee of the Department of Mechanical Engineering.

This research was supported in part by the faculty research initiation grant from Texas A&M University.

NOMENCLATURE

Bi	Biot number
CC	Constant current
C_P	Heat capacity
$\frac{dU}{dT}$	Entropic coefficient
h	Convective heat transfer coefficient
H	Height
I	Current
F	Faraday constant
k	Thermal conductivity
L	Length
m	Mass
η_{cell}	Over potential
$\dot{Q}_{gen}$	Total heat generation rate
$\dot{Q}_{rev}$	Reversible heat generation rate
$\dot{Q}_{irr}$	Irreversible heat generation rate
R_{in}	Internal resistance
SEI	Solid electrolyte interface
SOC	State of charge
τ	Time constant
T_0	Initial temperature of cell

T_{cell}	Surface temperature of cell
T_{fit}	Correlated (fitted) temperature
T_{∞}, T_{amb}	Ambient temperature
T_{mean}	Average temperature
U	Open circuit voltage
V	Terminal voltage

TABLE OF CONTENTS

Page

LIST OF FIGURES

Page

LIST OF TABLES

Page

CHAPTER I

INTRODUCTION TO LITHIUM ION BATTERIES

Introduction

One of the biggest problems the world population faces today is a large imbalance between energy demand and supply. Since our population is growing exponentially for last few decades, so does the energy demand to fulfil our needs. To satiate this high demand, we have been excessively using the fossil fuels, which includes coal, natural gas, petroleum, either directly by combustion (majorly in transportation) or to generate energy in the form of electricity involving many intermediated steps and use it for our needs (majorly in industrial sector and residential sector). In this process [1], by accumulating so much waste in our environment, we are disturbing the natural balance, which causes many catastrophes in turn endangering our own lives. So, one way to prevent all of this is to replace the use of fossil fuels with energy harvested from renewable (sustainable) sources which include solar energy, wind energy, tidal energy, geothermal energy. The idea seems to be plausible but the problem associated with the use of energy from any renewable energy source is that they fluctuate throughout the day, which renders them inefficient for our continuous demand. Another problem that arises with the shift of transportation (mostly ground transportation) from internal combustion engines (ICEs) to electricity produced from renewables is that we cannot have the entire setup that is required for energy conversion (from renewables to electricity) within our transport vehicle. So, the solution for all these problems might be just as simple as providing a storage device which can store the electricity generated from renewable sources during up time (when renewables sources are available) and use the stored energy during depletion time.

This makes the shift of transportation towards renewable energy by just equipping it with a storage device.

Figure 1. Battery module having several NCR18650 cells connected in parallel and series.

Batteries and their classifications

In this context [2], the storage device used is a battery as shown in Figure 1, which is a collective management (connected in series or parallel to obtain desired voltage and capacity) of a number of electrochemical cells which converts electricity energy from chemical energy or vice versa. The primary purpose of the battery is to power a device and storage and release of energy is realized by the flow of electrons and ions. The energy conversion process in the batteries happens in a single step as opposed to many intermediate steps involved in the electricity generation from the burning of fossil fuels and solar energy, wind energy etc., thereby increasing the energy efficiency.

Batteries can be classified [3] mainly into two types: primary and secondary batteries. Primary batteries are like use and throw type, as the electrochemical reactions associated with

it are mostly irreversible i.e. the reactions happening during discharge of the battery cannot be reversed. They are assembled in charged condition and then used e.g. Alkaline batteries, Silver oxide batteries, Lithium primary batteries, Mercury batteries and Zinc-carbon batteries. Secondary batteries are the ones which can be used again and again, since the electrochemical reactions associated with them are reversible i.e. the reactions that happen during the discharge of the battery can be reversed during charging by applying a certain voltage to the battery in opposite direction, so that battery can be charged/discharged for a number of cycles, hence named as rechargeable batteries e.g. Lead-acid, Nickel-Cadmium (NiCad), Nickel-metal hydride (NiMH), Zinc-air, Sodium-Sulphur, Lithium ion (Li-ion) and Li-air batteries.

Basic working principle of an electrochemical cell

A typical electrochemical cell consists of a positive electrode and a negative electrode immersed in an electrolyte solution with a porous separator between them. Usually, redox couples are employed as electrode materials i.e. when one material gets reduced the other material gets oxidized. The separator prevents the flow of electrons but allows positively and negatively charged ions to migrate from one electrode to other through the electrolyte. Both the electrodes are connected externally by conductive element through an external load, which provides the pathway for the flow of electrons between the electrodes. During discharge, oxidization takes place at negative electrode and electrons and positively charged ions are formed. Electrons flow from anode to cathode through the external circuit [3], creating a current in opposite direction while positive ions get dissolved in the electrolyte and move towards cathode through the separator. At positive electrode, the cathode material gets reduced by accepting electrons from the external circuit. The ions migrated to the cathode from anode gets reduced and precipitate. In rechargeable batteries, these reactions can be reversed by

applying a voltage in opposite direction during charging and entire process becomes vice versa, whereas in primary batteries these reactions are one way and cannot be reversed.

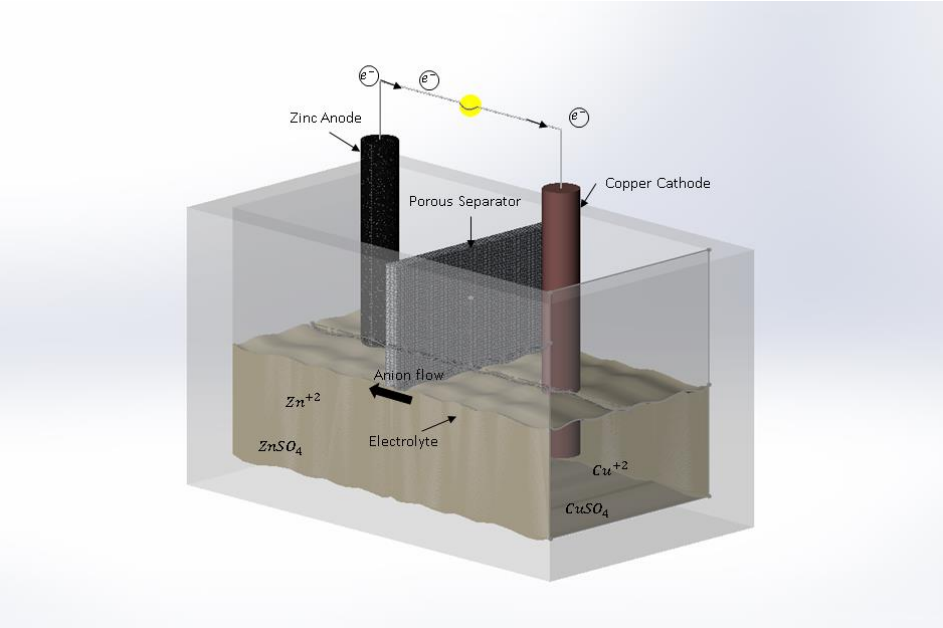

Figure 2. Schematic of an electrochemical cell.

Background and development

Primary batteries [4] have been around for more than a century while the first rechargeable battery based on Lead-acid was invented in 1859 by Gaston Planté and still in use today. Till 1940, the primary battery based on zinc-carbon was widely used because of its portability and robustness. Later it was replaced by a secondary battery based on Nickel-Cadmium, invented in 1899, and had been widely used in portable equipment from wireless communications to mobile computing. In the 1990s, Nickel-metal-hydride (NiMH) battery was commercialized supplanting the NiCad battery, having similarities to NiCad but being more environmental friendly than NiCad. Lithium, being the most electropositive element and the lightest metal, led to high energy dense systems which spurred interest among the researchers

around 1950s, eventually leading to the development and commercialization of a variety of primary Lithium cells in 1970s. Around 1980s, many efforts were put to develop the rechargeable Lithium batteries by using metallic Lithium as positive electrodes, but most of them were failed because of high reactivity of Lithium, inherent instabilities during charging and dendrite formation limiting the commercialization of these batteries. So, many attempts were made to modify the anode material and alloys of Lithium were used instead of Lithium metal, which solved the dendrite problem but limited the number of cycles due to the extreme volume changes during the operation. Later Lithium with insertion compounds were used as negative electrode material because of which anode potential increased and need to use higher potential insertion compounds for cathodes arose. This led to the usage of the higher voltage metal oxides (Li_xMO_2, where M= Ni, Co or Mn), which are more oxidizing than the previous compounds, as cathodes and are being used in commercial Li-ion batteries even today. Eventually, the discovery of highly reversible, low potential intercalation and de-intercalation of Li-ion in carbonaceous material led to the introduction of first commercial Li-ion battery based on $C/LiCoO_2$ by Sony in 1991.

Today [5], secondary type Li-ion battery is the fast growing and most promising battery chemistry and becoming prominent in most of the portable electronic devices and a wide variety of other applications due to their high-energy density, widely variable voltage, long cycle life, high charge and discharge rates, environmentally more benign than other chemistries. Unlike lead-acid and NiCad batteries, Li-ion batteries do not contain toxic heavy metals and they do not suffer from high self-discharge rate and memory effect of NiCad and NiMH batteries. The major short come with Li-ion batteries is that they require careful attention to safety. Overcharging, overheating, or short-circuiting a charged Li-ion battery can

result in fire or explosion. Research and development is going on to improve their safety, increase capacity, charge-discharge rate, and lifetime.

Basics of Lithium ion (Li-ion) batteries

'Lithium ion battery' refers to a diverse group of battery chemistries [5] with Li-ion in them and as with any battery, Lithium ion battery consists of three main components: positive and negative electrodes with a separator placed in between and together immersed in an electrolyte. Usually, Lithium metal oxide ($LiMO_2$) compounds (where M stands for metals such as Co, Ni, Mn etc.) are used as active materials in positive electrodes while lithiated carbons (Li_xC) are used as active materials in negative electrodes. These active materials are bonded to the current collectors (metal foils usually made of copper for anode and aluminum for cathode) and separated by a microporous polymer separator which isolates the electrodes electrically and allows diffusion of Lithium ions between the electrodes.

All Li-ion batteries use a process known as intercalation, in which Lithium ions are incorporated or inserted into the structure of the electrode active material and de-intercalation, in which Lithium ions are extracted from the structure of the electrode active material, during the operation of the battery. During the discharge process, the negative electrode is electrochemically oxidized and de-intercalation of Lithium from anode takes place while releasing the electrons. The Lithium ions formed at the negative electrode diffuses through electrolyte, across the separator and towards positive electrode. The electrons released at the negative electrode moves through the current collector, then through the outer circuit towards the positive electrode which accepts electrons. The positive electrode gets reduced by accepting electrons and intercalation of Lithium ions into cathode active material takes place. And during charging, the entire process is reversed, the cathode active material gets oxidized

releasing the electrons and de-intercalation of Lithium ions takes place from cathode. The electrons travel through the external circuit and Lithium ions through the electrolyte towards negative electrode, where negative electrode is reduced by accepting the electrons and intercalation of Lithium ions takes place.

Figure 3 shows schematic of Li-ion cell with Li_xC_6 as anode active material (negative electrode) and $Li_{1-x}NiMnCoO_2$ as cathode active material (positive electrode). During discharge, the graphite electrode gets oxidized releasing electrons and de-intercalating Li-ions which moves towards $LiNiMnCoO_2$. On the other half, $LiNiMnCoO_2$ gets reduced by accepting the electrons and intercalates Li-ions in its structure. This process reverses during the charge and is as shown below.

Reaction at positive electrode

$$Li_{1-x}NiMnCoO_2 + xLi^+ + xe^- \rightleftharpoons LiNiMnCoO_2$$

Reaction at negative electrode

$$Li_xC \rightleftharpoons C + xLi^+ + xe^-$$

Net electrode reaction

$$Li_xC + Li_{1-x}NiMnCoO_2 \rightleftharpoons C + LiNiMnCoO_2$$

The intercalation of Li into graphite occurs in various stages [6]. A first polarization of graphite electrodes in any polar aprotic Li salt solution consumes irreversible charge for reduction of the solution species and forms a passivating film known as Solid -Electrolyte Interface (SEI) that prevent any further irreversible process and provide metastable conditions for the Li_xC_6 stages that are formed during Li insertion into graphite, all of which are highly reducing agents. To account for this loss, Li-ion battery contains excess of Li in its cathode.

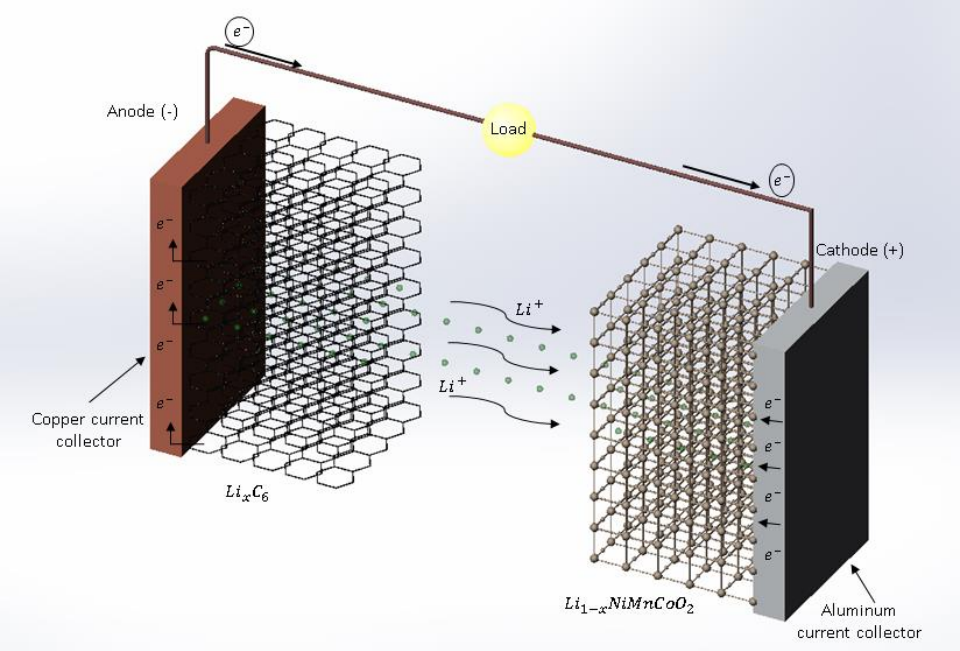

Figure 3. Schematic of Li-ion battery.

As role of electrolyte is to act as a medium for the transfer of ions between the two electrodes, it should possess some important characteristics when using in Li-ion batteries:

(i) Should be a good Li-ion conductor and electronic insulator

(ii) Should be stable over the operating voltage window

(iii) Should be chemically compatible with the cell components and electrodes

(iv) Should be thermally stable over a wide range of temperatures and

(v) Should have good transport properties.

Usually [6], Lithium salt (Lithium hexafluorophosphate (LiPF6)) dissolved in an organic solvent (mixture of ethylene carbonate (EC) and either dimethyl carbonate (DMC), ethyl methyl carbonate (EMC) or diethyl carbonate (DEC)) is used as a basic standard electrolyte in Lithium ion batteries. $LiPF_6$ passivates and protects aluminum current collectors. As the conductivity of non-aqueous electrolytes used in Li-ion batteries is less compared to

aqueous electrolyte, the electrodes stacks are made very thinner which decreases the distances which the ions should conduct and this also increases the volumetric and gravimetric power densities.

Types of Lithium ion batteries

Based on chemistries

As of present day [7], the most widely used anode active material in Li-ion batteries is carbon based and research is going on to find alternative materials with both higher capacities and slightly more positive intercalation voltages. Coming to cathodes, the most widely used active material is based on Li with other metals like Cobalt, Manganese, Phosphate and sometimes electrochemically inert cationic substitutes like Ni, Al, Ga, Mg, Ti, etc. are introduced to stabilize the layered structural framework. Li-ion batteries are often named after its active materials, like LCO for Lithium Cobalt Oxide, NMC for Lithium Nickel Manganese Cobalt oxide, LMO for Lithium Manganese Oxide, LFP for Lithium Iron Phosphate, NCA for Lithium Nickel Cobalt Aluminum oxide, LTO for Lithium Titanate etc. Each of these chemistries have their own advantages and disadvantages.

$LiCoO_2$

This cathode has layered structure. One of the main advantages of this system is its high-energy density which made it a popular choice for applications in mobile phones, laptops and digital cameras. But the major drawbacks of this chemistry are its relatively low cycle life, low thermal stability, low rate capabilities.

$LiMnO_2$

This system has three-dimensional spinel structure, which give rise to low internal resistances and improved rate capabilities. This spinel structure has also good thermal stability, but has lower capacity compared to LCO system.

$LiNiMnCoO_2$

High specific energy of Nickel and low internal resistance of Manganese spinel structure combined with reduced Cobalt content offers low cost, long life and inherent stability which makes them preferable over Cobalt, Nickel or Manganese structure alone.

$LiFePO_4$

This uses phosphate as cathode material and offers low resistance, high current rating, long cycle life, enhanced safety, good thermal stability and tolerance to abuse. This is cost effective considering its cycle life, but has lower voltage which reduces its specific energy to lower than that of LMO.

Based on physical formats

With the wide spread of Li-ion batteries into various sectors [8], the applications became widely varying, which necessitates to manufacture them in various sizes, shapes and forms. Some of the most commonly used standard forms of Li-ion batteries are cylindrical cells, button or coin cells, prismatic cells and pouch cells as follows.

Cylindrical cells

The most widely used form among both primary and secondary batteries are cylindrical cells. It has many advantages over other forms of cells. These forms are in use for a long time, production lines must have been optimized, so results in less cost per kWh energy produced. They are also very easy to manufacture, have good mechanical stability due to tight wounding

and metal encasing. But when cylindrical cells are placed together, there is lots of space between the cells, which give rises need to efficient space management in the battery, usually thermal regulation systems are installed in these spaces.

Figure 4. CGR18650CG cylindrical Li-ion cell.

The most commonly used construction in Lithium ion cell is spirally wound electrodes structure also called as jelly-roll or swiss-roll structure. This construction is used to increase the current carrying capacity of the cell by increasing the active surface area of the electrodes by making them into thin strips and rolling them tightly, where the size of the electrode cannot be increased to increase the active surface area due to the limitations on the cell size. This also decreases the conducting distance for ions, thereby decreasing the internal resistance of the cell.

But the room for electrolyte in the cell is greatly reduce now, since most of the space is occupied by the electrode sheets and separator, so the potential energy storage of the cell is reduced. This cylindrical structure is not limited to Li-ion batteries but also widely used in lead

acid batteries, NiCad and NiMH batteries. These are generally used in laptops, medical devices and large cylindrical cells are used in electric vehicles. Most of the cylindrical cells include various safety mechanisms: 1) Positive thermal coefficient (PTC) protection, 2) Venting mechanism or pressure relief mechanism.

Button or coin cells

Figure 5. Coin cell.

As the name suggests they are very small compared to other forms of cells and mostly used in portable devices like watches, calculators, medical implants, hearing aids, memory backup devices. These usually do not have any safety mechanisms like cylindrical cells. They have relatively high capacity but deliver low power. Both primary and secondary batteries are available in this format but most of them are primary batteries. Rechargeable batteries are also available in the same sizes but with lower capacity than primary versions.

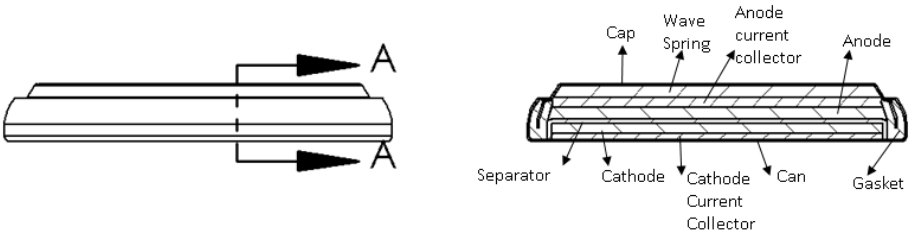

Figure 6. Cross section of a coin cell.

Prismatic Cell

Prismatic cells have advantages of having thinner profile and effectively use space due to the rectangular shape or flattened spiral contained in a rectangular can, giving more flexibility in designing. They are more commonly used in small electronic devices such as mobile phones, tablets and laptops. There is no standard format for this battery and every manufacturer has their own design.

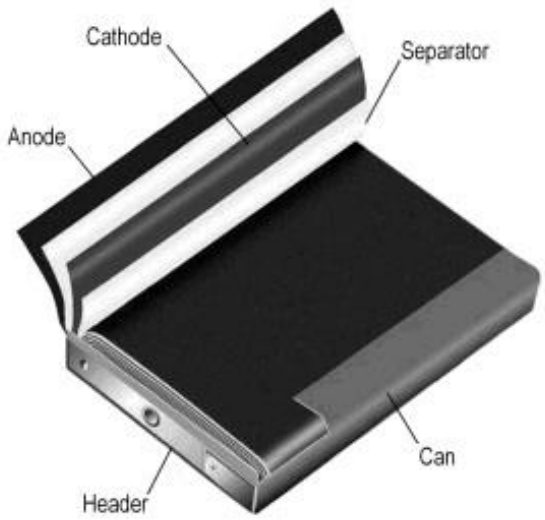

Figure 7. Cross section of a prismatic battery [8].

Prismatic cells are also available in large formats with capacities of 20-50 Ah, primarily used for electric powertrains in hybrid and electric vehicles. They require thicker walls to have good mechanical stability which results in high manufacturing cost, capacity drop, low energy density, more vulnerable to swelling, ineffective thermal management and short cycle life compared to cylindrical formats.

Pouch cells

Figure 8. Pouch cell [8].

Pouch cells are mostly used for Li-polymer cells with solid electrolytes where electrodes together with solid electrolyte are stacked in layers and enclosed in foil envelope, eliminating the metal enclosures, reducing weight and effectively using the space than any other cell format. The conductive metal foil tabs are welded to electrodes and brought outside completely sealed. Due to lack of mechanical rigidity, these cells are more prone to expansion with rise in temperature and allowances should be provided for expansion in battery compartments. These are most commonly used in consumer, military and automotive applications. No standard size exists and every manufacturer has its own design. Due to soft outer cover, these cells are prone to mechanical damage (punctures etc.), especially high during the swelling of the cell, and any sharp edges are to be avoided in proximity.

Common problems associated with Lithium ion batteries

Lithium ion battery [10] requires low maintenance and causes little harm when disposed. Despite many advantages over other chemistries, it still has its own drawbacks. Some

of the problems associated with Lithium ion batteries are due to faulty design and materials, improper tolerances used, inadequate knowledge of design engineer and inadequate equipment which all can be greatly reduced by carrying thorough quality checking. Other problems can occur randomly during operation due to abuse like over charging and over discharging, operating at higher rates than recommended, operating at subzero temperatures and high temperatures, crushing, vibrations, ageing mechanisms, external factors (includes sensor failures, circuit interrupter failure, fan or pump failures, loss of cooling fluid, incorrect or missing BMS messages, BMS failure, charger failure).

Causes of cell failure

Some of the cell failures associated with Li-ion batteries [10] are due to: exhaustion of active materials due to ageing, decomposition of the electrolyte due to overheating or over voltage, electrode plating due to low temperature operation or high rates of operation, increase in internal impedance and capacity loss due to cycling, increased self-discharge due to change in morphology of electrodes, pressure build up in the cell, penetration of the separator and short circuit due to dendrite growth, uneven separators which can develop local hotspots and weakens the separator causing short circuits, contamination, softening of separator due to overheating, swelling, overheating and thermal runaway. So, the precautionary methods must be incorporated while designing battery packs and any applications that uses cells to reduce the catastrophic failures like thermal runaway caused by external factors that are beyond the manufacturers control.

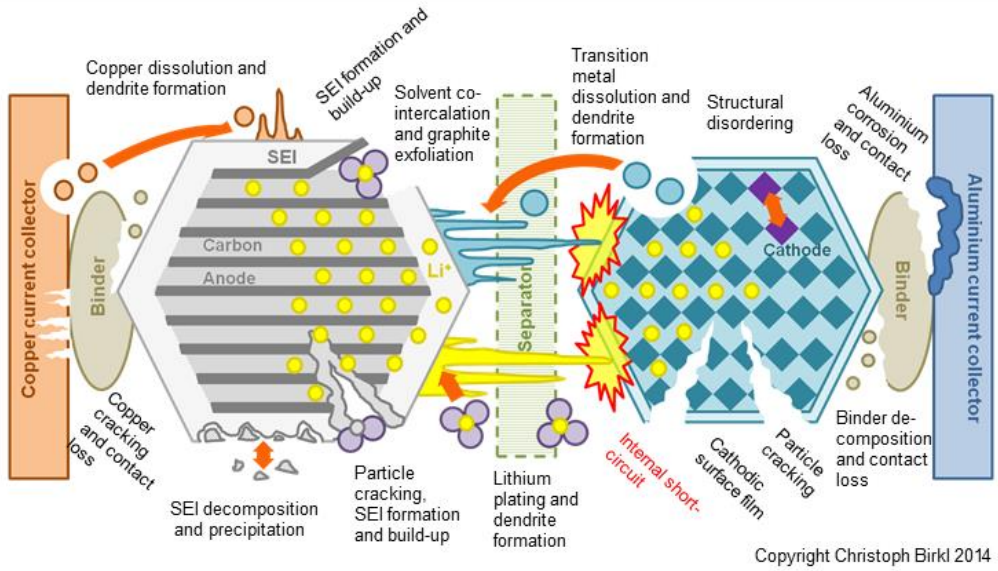

Figure 10. Lithium dendrites piercing into separator and causing short circuit in Li-ion batteries [9].

Aging is a problem associated with many battery chemistries, so does with Lithium ion. Due to unwanted chemical reactions, some capacity deterioration occurs gradually and eventually results in the failure of the battery and usually occurs whether the battery is in use or not. This may occur due to the passivation, corrosion, chemical loss through evaporation, change in morphology of active chemicals, electrode or electrolyte cracking. New enhanced chemical combinations are being introduced to fight the age-related degradation. Storage at low temperatures around 15^{o}C and partial charge during storage can also help in slowing the aging process.

Safety hazards and protective measures

There will be some sort of safety issues [12] associated with any type of energy storage device, so does the same goes with Li-ion batteries. But these risks can be greatly reduced if the manufacturers of those devices meet certain safety requirements. Even though highly cautious, failures are bound to happen, since millions of batteries being produced and used. A

case where one in 200,000 failure rate triggered the recall of almost six million Lithium ion batteries and manufacturer in question says it is due to the microscopic particles meeting parts of the battery which happens very rarely and impossible to eliminate due to the complex manufacturing and assembly techniques. Also, as we go for denser batteries, the separator thickness decreases and is more prone to damage in the presence of particles. The older lower capacity batteries can withstand a nail penetration test, whereas the new higher capacity batteries will ignite during the same test so rendering this test useless against high energy density batteries. Since Li-ion cells using conventional metal oxides are nearing their theoretical specific energy, the focus is shifting towards enhancing the safety and calendar life of batteries.

The safety is usually achieved by employing many methods: optimizing the amount of active material to have optimal energy density and safety, inclusion of variety of safety mechanisms within the cell like adding the electronic protection in the circuit of battery pack, built-in PTC device to protect the cell from high current surges, CID to protect if there is certain pressure rise and safety vent which allows a controlled release of gas if there is rapid rise in pressure inside the cell. By employing electronic protection circuits, we can limit the peak voltage (overcharging) and lower voltage (over discharging), temperature extremes during normal operational rates by which we can virtually eliminate Lithium plating and capacity fade. But if the problem rises due to inherent defect in the cell, these protection mechanisms cannot prevent the cell from failure. Since we use so many batteries connected in series in EVs and HEVs, the mismatched capacities of cells can result in overcharge of lower capacity cells causing Lithium plating leading to cell failure. So instead of monitoring overall pack voltage,

individual cell voltage should be monitored for safe operation [12]. Most of these failures triggers the temperature rise which eventually leads to the failure of the cell.

Effect of temperature on Lithium ion batteries

Heat is always the enemy of the battery [5]. Too much heat or too much cold is not good for them, and optimal conditions should be maintained for their good operation and longer state of health. Elevated temperatures in battery triggers unwanted exothermic reactions and they further rise the temperature triggering even more deleterious reactions causes rapid uncontrollable temperature rise leading to thermal runaway causing fire and explosion. This process occurs in following steps: First the passivating solid electrolyte interface (SEI) layer on the anode breaks down due to high temperature or penetration and reaction between anode and electrolyte (which occurs during formation) occurs now uncontrollably at these higher temperatures and heat builds up breaking the organic electrolyte and releasing hydrocarbon gases and reaching temperature beyond their flash point. At this point, due to unavailability of oxygen fire doesn't start yet. Then the separator melts short circuiting the electrodes, and eventually breaking down the metal oxide cathode, rising the temperature and pressure even more and releasing oxygen which enables the burning of gases previously released and both temperature and pressure rises rapidly leading to explosion.

While all batteries [5] can present safety hazards if used improperly, Li-ion batteries are especially sensitive to proper handling and treatment. Li-ion batteries can vent electrolyte, catch fire, or explode if overcharged, overheated, or short-circuited. Overheating causes the negative electrode material to react with the electrolyte, causing venting or fire. Charging of Lithium ion batteries is more delicate than discharging [5], hence we should be careful while charging them. Most Li-ion batteries cannot be charged at ambient temperatures below 0°C or

above 45-50°C. At higher temperatures, the Lithium ion batteries have increased performance but their life is greatly reduced. Charging at high temperature (even storing the battery at high temperature) will cause capacity fade, charge acceptance is greatly reduced which decreases cycle life and may present a safety hazard due to unreliable full charge detection. Storing battery at higher temperatures at high state of charge (SOC) causes even more capacity fade than low SOC because of increased rate reactions. Phosphate-based batteries may have somewhat better high-temperature performance than Li-ion and Ni chemistries.

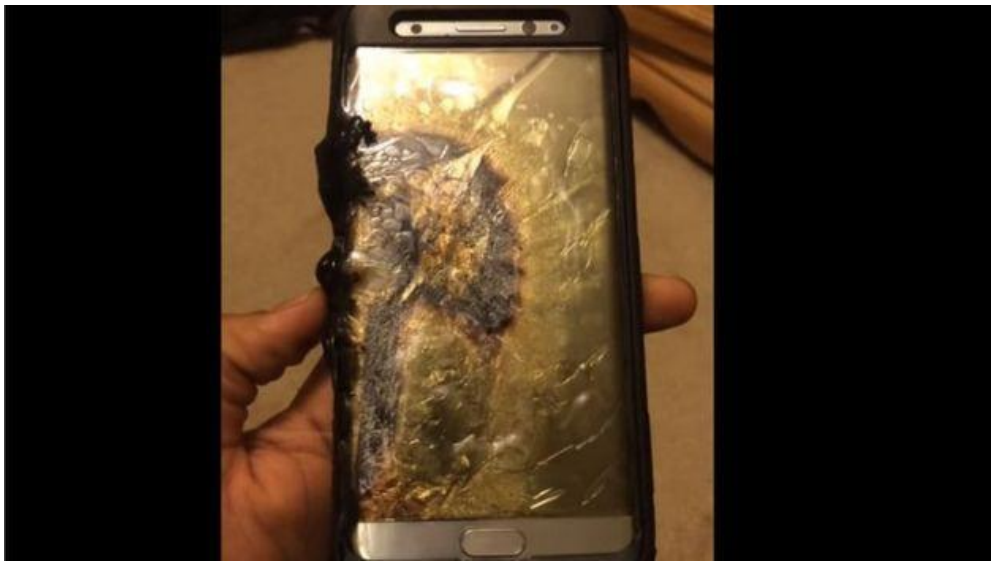

Figure 10. Explosion of Lithium ion battery [10](Ariel Gonzalez).

Charging Li-ion batteries at lower temperatures should be done at extremely lower C-rates and should be avoided if possible. Although battery appears to be charging normally at low temperatures, Lithium plating may occur leading to the growth of Lithium metal dendrites, which can penetrate separator resulting in an internal short circuit, destroying the battery and potentially causing a fire. Mild short might cause elevated self-discharge which results in small

heat buildup but if enough current flows, the heat built up can damage insulation and create an electric short, rising the temperature rapidly to around 500^{o}C leading to thermal runaway. Ensuring that the temperature remains within the acceptable range is especially important for products that may be charged outdoors where the ambient temperature may be too high or too low.

Typical Lithium ion battery generates [5] heat even if it charges and discharges in normal operating conditions, but does not lead to thermal runaway, if properly cooled. But if it is not properly cooled heat accumulation takes place and eventually leads to higher temperatures causing thermal runaway. If the battery management system contains a temperature sensor in contact with the battery, it can stop charging before thermal runaway starts. If a cell goes to thermal runaway, it can easily propagate to the neighboring cells and leads them to thermal runaway in their own time. So, care should be taken by providing certain dividers between cells isolating them from each other. The Li-ion batteries with cobalt based cathodes can temperatures up to 130^{o}F whereas the manganese based cathodes can withstand temperatures up to 250^{o}C. Higher SOC can trigger thermal runaway at lower temperatures compared to lower SOC. So, the onset of temperature can depend on battery chemistry, SOC and abuse condition.

Thermal management

So, now we know that thermal management plays a crucial role in cell and pack design and Lithium ion battery needs optimal temperature conditions for optimal performance, life and safety, we should know what methods to be employed to achieve that in various applications. Though there are myriads of causes for temperature fluctuations in batteries, we can solve this problem by temperature of each cell in the pack by employing methods

depending on application which may involve fins, fans circulating air (cool or hot depending upon purpose), phase change materials (PCM) which can absorb significant amount of heat without change in its phase (high latent heat). The types of cooling systems can be classified as active and passive systems depending on how we are controlling the temperature, air or liquid cooling depending on the physical state of coolant we are using (usually we employ air cooing, conditioned from cabin, for smaller packs and liquid cooling, system connected to radiators, for large packs) and based on type of temperature control mechanisms used. These all thermal management systems can be used in combination with complex algorithms for detecting the exact state of individual cell like temperature, state of charge etc., and regulating the flow of coolant and temperature of coolant can achieve high level of thermal management which might be trivial in simple applications but plays an important role when it comes to high energy storage (automobile, grid storage) with limited space and highly fluctuating operating conditions.

Passive thermal management refers to cooling or heating without any external aid and solely based thermodynamics and heat transfer from component to the coolant. There is a limit on the amount of heat transfer (cooling or heating) that can be provided by these systems, which usually depends on efficiency of heat transfer from the cell (depends on heat transfer coefficient) and the thermos physical properties of the cell components. If the ambient temperature is not optimal and is too cold or too hot, the battery packs may suffer because of insufficient heating or cooling, since, the heat transfer also depends on the ambient temperature conditions in this system. But these systems eliminate the use of many other mechanical components that are involved in active thermal management thereby decreasing the weight,

space required and the cost involved is very low compared to active systems, so these are most commonly used in portable applications where space, weight and cost are crucial factors.

Active thermal management refers to achieving cooling or heating by taking external aids like fans to induce forced convection either by air or liquid and heaters during cold temperature operations. These systems give far better heat transfer results than passive systems. But increased number of components leads to both increased weight, space and cost, which limits their application, since they become cumbersome where there are limits on space and weight.

Preventing excess rise in temperatures by employing various air cooling or liquid cooling methods. Each of the cooling types has its own advantages and disadvantages. Liquid cooling is more effective and retains heat for longer than air cooling but care should be taken while using liquids to prevent corrosion, accidental short circuits when used in direct contact with batteries. Liquid cooling might become quite costly than compared to air cooling since air cooling does not have any special requirements and can be directly blown over batteries to achieve cooling. We can prevent most of the hotspots developed in the battery pack by absorbing the heat generated from all batteries in the pack and distributing it uniformly, which can be attained by employing a highly conducting material like aluminum, which absorbs heat and distributes heat quickly. Internal cooling channels can be employed inside the battery packs which can absorb and dissipate the excess heat produced during the thermal runaway conditions.

During extremely low temperatures, the temperature of batteries could be raised by heating it externally (convective heating) by employing heaters, heat produced from engines in case of HEVs, or internally (self-heating) by providing high external load on battery

(drawing high current which increases ohmic heating), applying high current pulses. Smart chargers can also be employed to charge batteries at certain C-rate depending on the temperature of the battery. During charging at low temperatures, the internal resistance of the battery comes into act giving rise to heat which can increase battery temperature.

To make employment of any of these methods or mechanisms feasible we should first know the amount of heat generated during the operation of a cell (to which we want to design thermal management), under various operating temperatures, various cycling rates, various state of charges and state of health. Then we can correlate these heat generation results with parameters of the cell and temperature of the cell and create a thermo-electrical lumped model and incorporate it into battery thermal management system (BTMS) which can predict the amount of heat generated at any given time by having certain fixed standard parameters (thermo-physical properties) and certain in situ measurements (temperature, voltage and current measurements).

CHAPTER II

THEORETICAL BACKGROUND

With recent advances, Lithium ion batteries have been replacing other battery chemistries like NiCad, NiMH etc. and have been extensively used in most of the portable applications like laptops, cell phones and other consumer applications because of their high energy density, low self-discharge, lighter weight, no memory affect, high open circuit voltage etc., They are now being considered as a good candidate for high energy storage applications like power grids, Electric vehicles (EVs), Hybrid electric vehicles (HEVs) and Pug-in hybrid electric vehicles (PHEVs) and are expected to replace lead acid batteries and Ni-based battery chemistries. This calls for the need to research key issues associated with scaling up of Li-on batteries to high capacity energy storage.

Most of the research on Li-ion batteries is focused on developing materials for increasing specific energy, capacity, power and cycle life and not much attention has been paid to thermal aspects of the battery, which is of prime importance in scaling up of Li-ion batteries for high energy applications. Operation of Li-ion batteries inherently generates heat due to electro-chemical reactions happening inside the cell, electrical resistances and other polarization resistances developed during operation and heat buildup takes place inside the cell owing to the thermo-physical properties of the cell components. Adding to this, the higher ambient temperature might lead to the increased cell temperature and the battery cell is prone to self-sustain some undesired exothermal reactions when the temperature exceeds certain threshold which causes rapid, uncontrolled temperature rise in cell leading to catastrophic failure (thermal runaway) of the cell and may also propagate to other cells in the battery pack. Also, high temperature operation leads to accelerated capacity fade, decreased cycle life along

with safety issues. So, care should be taken to maintain the optimal temperature range and temperature uniformity for individual cell and throughout the entire battery pack.

The temperature of the cell can be kept in control either by decreasing the inherent heat generated in the cell by improving the design of the electrode and optimal selection of materials for cell components or by cooling externally with battery thermal management system (BTMS), of which we will focus on the latter method in this study. Designing a proper BTMS needs the prediction of amount of heat generation in the battery for given operating conditions and state of the battery. This requires a detailed thermal analysis and development of thermal and electrochemical models coupled with each other, which can predict the amount of heat generation. Since thermal management of Lithium ion batteries is gaining importance very recently, there is a very little research done on this aspect of Lithium ion batteries.

Zhang [11] developed a coupled electrochemical-thermal model to analyze the different sources of heat generation during the discharge of a cylindrical Lithium ion battery. The cell is modeled with thin layers of cathode, separator, current collector and anode rolled up into spiral on a central mandrel [12] and having Lithium manganese oxide ($LiMnO_4$) as positive electrode, graphite meso carbon micro-bead (MCMB) 2528 as negative electrode and $LiPF_6$ in a solvent mixture of propylene carbonate/ethylene carbonate/dimethyl carbonate as electrolyte [13]. The mathematical model includes electrochemical kinetics, solid phase Lithium transport, Lithium ion transport in electrolyte, charge conservation/transport, energy conservation/dissipation and heat transfer [14-18] and is validated with existed experimental data. The discharge process was simulated with cycling rates of 0.5C, 1C and 1.7C. Contribution of three sources of heat generation ohmic heat, polarization heat and reaction heat were computed during the discharge process which shows that the contribution of ohmic heat

is largest towards the total heat, next to it is reaction heat and third is heat due to active polarization. The Lithium ion concentration and its gradients are recognized to have effect on ohmic resistance and active polarization and therefore important factors of heat generation. The temperature towards the end of the discharge is found to increase with increasing both the separator and electrode thickness.

Chen, et al. [19] developed a two-dimensional thermal model which accounts for the hollow core, spiral, contact layer and the case in a battery to avoid deviations due to improper approximation of the complicated spiral geometry. The energy balance equation proposed by Bernardi, et al. [20] is used and the model has the flexibility to adopt to various boundary conditions. Results from this work shows that maximum temperature of the battery is not located exactly at the center but in the circular region near the core and the temperature difference between surface and core increases with increase in number of spirals and radius of the battery. Also, the results show that heat dissipation can be significantly improved by enhancing the surface emissivity and in forced convection with parallel flow effectiveness of convection decreases with increase in radius.

Chen and Evans [21] carried out thermal analysis of Lithium ion batteries during charge/discharge and thermal runaway with a mathematical model. The results indicate that during normal battery operation, battery temperatures are unlikely to reach the onset temperature of thermal runaway, although heat may not be dissipated out of a large cell stack during high rate discharge [22] and if the battery is continuously cycled at higher rates, significant heat accumulation may be caused within a battery which may increase temperature to the onset of thermal runaway.

Sato [23] carried out thermodynamics experiment and analysis for Lithium ion batteries and confirmed that heat absorbed and rejected depends on charging and discharging respectively. The heat generation was divided into three types: reaction heat, polarization heat and joule heat. This is verified by comparing thermodynamics calculations with the experimental data of heat generation.

Eddahech, et al. [24] investigated thermal behavior of high-power Lithium cells using an ARC calorimeter [25, 26] to measure the heat generated by the Lithium-ion cell during charging and discharging at various C-rates. Total heat generation in the battery is related to both joule heating which is due to internal resistance and entropy change due to electrochemical reactions that occur during charging and discharging [27-31]. Entropy was measured using both potentiometric and calorimetric methods, to quantify the reversible heat component and the results confirmed its significant dependence on SOC variations [32]. The influence of entropy change, on heat generation was less marked at higher C-rates, resulting in a larger irreversible heat component during charging and discharging at high current rates.

Hatchard, et al. [33] developed a predictive model for oven exposure testing, using reaction kinetics that have been developed for electrode materials with electrolyte exposed to high temperature, and thermal properties of cells from literature [34, 35]. It can be used to determine the performance of cells made from new materials in abuse test without producing test batches of cells. This model can also be used to test design changes to cells such as increase in radius or capacity and to predict the effects of changing cathode reactivity, changing to a higher or lower surface area carbon anode.

Khateeb, et al. [36] reported the experimental results along with the simulation results for a Li-ion battery in electric scooter applications. The four modes of heat dissipation are

considered: a) natural convection, b) presence of aluminum foam heat transfer matrix, c) use of phase change material (PCM) [37, 38], and d) combination of foam and PCM. Using foam or PCM alone resulted in lower temperature than without either of them but are not effective for the use in harsh and abusive operating conditions, whereas using PCM and foam together resulted in the lower temperature of the module and individual cells than that of natural convection without them as well as effective during hot summer conditions and other harsh thermal conditions.

Al Hallaj, et al. [39] developed a simplified 1-D thermal model which uses lumped parameters [40] to simulate the temperature of Li-ion cell during discharge. This model uses the heat generation parameters of the Sony US18650 cell [41, 42], which are established experimentally. The temperature profiles for scaled up cylindrical Lithium ion cells of 10 - 100 Ah capacity are simulated with this model at various operating conditions and cooling rates. Cooling rates were found to have strong effect on the cell temperature for all discharge rates. At higher cooling rates, the temperature gradient was found to be significant, whereas at lower to moderate cooling rates, the cell behaves as a lumped system.

Forgez, et al. [43] developed a lumped-parameter thermal model of a cylindrical $LiFePO_4$/graphite battery. The internal temperature of the battery was measured by inserting a thermocouple into the cell under inert atmosphere to determine the input parameters for the model. Using this model with the surface temperature measured using a thermocouple, the internal temperature of the battery could be determined with an error less than 1.5^{o}C.

Jeon and Baek [44] employed a model to simulate thermal behavior of cylindrical Li-ion battery during discharge [45-50]. The transient model developed equations by assuming the total heat generation to be due to joule heat and entropy change for all the cell components

[20]. The comparison with experimental data showed similar tendency in the temperature profile as that of simulated one. For lower discharge rates, the highest temperature was observed at low SOC due to entropic heat dominant at lower SOCs [41, 46, 51] and at higher discharge rates the temperature increased linearly along discharge time which is due to joule heat being dominant [45]. The maximum temperature was observed in this case is inside the cell, but the difference between the maximum temperature and surface temperature was small [12].

Nieto, et al. [52] developed a thermal model for predicting heat generation in a large 10.5 Ah pouch type Li-ion cell based on the calculation of heat generation from internal resistance measured experimentally [53, 54] and the entropic heat coefficient without involving any complex electro-chemical models [43]. Predictions from the model are compared with experimental adiabatic calorimetry data. This model is very versatile; it can calculate the heat generated by the cell at any current condition, SOC and temperature making it possible to understand how design and operation variables affect the thermal behavior of the cells tested during charge and discharge processes.

Al-Hallaj and Selman [55] investigated the use of phase change material (PCM) in the thermal management of Li-ion batteries in EVs/HEVs as a passive cooling system [56]. During the discharge of the battery, the PCM integrated in the battery acts as a heat sink. When the temperature of the cell exceeds that of the PCM during discharge, the heat starts flowing into the PCM and PCM melts absorbing the heat maintaining the constant temperature and when the temperature of the cell decreases during charging, the heat flows from the PCM to the cell. The remaining heat from the PCM is dissipated to the surroundings. It concludes that the PCM material should be chosen such that its operational temperature is more than the temperature

of the surroundings. To accommodate for extra-cold climates, a parallel heat conduction path may be designed into the PCM system.

Pals and Newman [57] [58] developed two models to predict the thermal behavior of the Lithium/polymer battery. One of them is the one-cell model and one dimensional model for predicting the thermal behavior of the Lithium negative electrode/solid polymer/separator/insertion positive electrode cell. The other is the cell-stack model which is one dimensional model that uses heat generation rates calculated by the one cell model to predict temperature profiles in cell stacks. The one cell model is based on the model of Doyle, et al. [15] with the addition of an energy balance in the form given by Bernardi, et al. [20]. Heat transfer to the surroundings is considered by defining a position dependent heat transfer coefficient for various cells in a cell stack.

Doyle, et al. [15] presented a full cell model for galvano static charge and discharge of a Lithium anode, solid polymer electrolyte, and insertion composite cathode [59] using concentrated solution theory. This model includes a wide range of polymeric separator materials, Lithium salts, and composite insertion cathodes [60]. The velocity of the polymer is assumed to be zero and volume changes in the system are neglected. Film formation at the Lithium/polymer interface also is neglected. The composite cathode is modeled using porous electrode theory with both kinetic and diffusional resistances to solid phase transport. The results of a simulation of the charge/discharge behavior of the Li/PEO_8-$LiCF_3SO_3/TiS_2$ system are presented.

Bernardi, et al. [20] developed a general energy balance for battery systems which is useful for estimating cell thermal characteristics. The model incorporates the changes in the temperature of the cell due to electrochemical reactions, phase changes, mixing effects, and

joule heating in a complete and general manner. The energy balance is applied to the mathematical model of LiAl/FeS cell discharged through two different reaction mechanisms. The results show that the processes involved in the heat generation of a cell may be complex, so the application of a general energy balance equation is useful.

Chacko and Chung [61] developed a transient three-dimensional electro-thermal cell model based on finite element method, to predict the electrical and thermal behavior of a Li-ion polymer. This model is validated based on experimental data. The cell level thermal behavior under stressful conditions was predicted with the model. The cell temperature and the cell voltages are accurately predicted using this model.

Somasundaram, et al. [62] developed a 2-D coupled thermal-electrochemical model for commercially available spiral-wound Li-ion battery [63] and analyzed the effect of the geometry and passive thermal management with PCM during discharge[64-66]. The depletion of the active material was found to be larger at the outer end of the spiral for the positive electrode and at the inner end of the spiral for the negative electrode than at the remaining parts, where it is utilized uniformly. The PCM is found to have reducing effect on the average temperature of the battery at higher discharge rates.

Taheri, et al. [67] developed a three-dimensional closed form analytical model [68] based on integral transformation technique [69] to investigate the thermal response of the batteries. This model accounts for multi-dimensional heat conduction, orthotropic thermal conductivities, time dependent and temperature dependent heat generation terms, convective-radiative boundary conditions [12, 70, 71]. The model is verified with the numerical data. The temperature rise in a prismatic li-ion polymer cell, during discharge process, was studied with this model by approximating the transient heat generation rate from the electrical performance

of the battery. Natural convection was found to be effective in keeping lower temperatures from low to moderate discharge rates, but forced convection or liquid cooling is required for more aggressive discharge conditions.

Jeon [72] developed two FEM based models and simulated to provide the thermal behavior during charge and discharge. Commercially available cylindrical (18650) battery was modeled in this study. The porous electrode model is simulated to estimate the Li content inside the particles [48, 73-76] and this value is used to simulate the transient thermo-electric model to predict the temperature distribution inside the cell [44]. The results suggest that the temperature during discharge is higher than that during charge and the temperature difference between charge and discharge decreases as we go for higher C-rates. The maximum temperature was observed below the center of the cell and the difference between maximum temperature and the surface temperature was small. At lower C-rates the charge temperature increased until of middle of charge and then decreased whereas during the discharge the temperature along the discharge time. At higher C-rates the temperature increased with both charge/discharge time.

Marcicki and Yang [77] presented a real-time estimation technique that is capable of estimating heat generation during cycling for Li-ion cells, by using a lumped energy balance combined with Kalman filtering to design an input observer. The method is validated for the reversible component of heat generation by comparing the values estimated during cycling with those obtained during characterization experiments. Although the method has been applied to the reversible component of cell heating, it is equally applicable to other heat sources. The method is capable of near real-time applications with minimal computational cost,

which presents the opportunity to incorporate estimates of the entropy of reaction in battery management systems.

Rao and Newman [78] developed a new calculation method for the heat generation rate, based on the general energy balance for insertion battery systems by using enthalpy potentials. An alternative method based on local heat generation also gives a consistent result when explicit effects of a concentration gradient on heat generation by an electrical current are neglected. The two methods give close results if the insertion electrode has a smooth OCP. On the other hand, a varying slope of OCP promotes a large difference between them. For a dynamic discharge, the conventional method significantly deviates from the present method and produces significant errors.

Thomas and Newman [79] presented two methods for computing the heat of mixing, one based computational method whereas other based on analytical approximation. Heat of mixing is termed as the heat produced during the relaxation of concentration gradients after a sudden interruption of current, in an electrochemical system. The magnitude of the heat of mixing is usually neglected in materials with sufficient transport properties to provide acceptable battery performance, except for heat of mixing within the insertion particles with large particle radius.

Drake, et al. [80] presented an experimental method for having in situ heat generation rate measurements based on the thermal response of the cell during higher discharge rates. This is based on simultaneous determination of the amount of the heat stored and the heat lost from the cell, by measuring the cell temperature and heat flux and it does not consider any underlying heat generation mechanisms. This method uses the volume-averaged cell temperature from only two discrete, point measurements, of a dried cell, to determine the

internal temperature of a similar undrilled cell. Strong dependence heat generation rates on C-rate was indicated and is in excellent agreement with theoretical models [81].

Saw, et al. [82] developed a pseudo 2-D coupled thermal - electrochemical model to investigate the charge and discharge behavior of the commercial 18650 Lithium Iron Phosphate battery. The cell was dissected to obtain the physical dimensions of the cell components. The layer structure of the spiral wound, cylindrical casing, gasket and heat shrink wrapping were modeled to understand better the temperature across the cell and verified with experimental results. Results suggest that reaction heat was the main heat source and contributes 85% of the total generation during charging and discharging of the cell. The electrical contact resistance between the connectors and terminals of the cell was found to have a huge effect on the temperature gradient across the cell.

Hong, et al. [41] measured the heat dissipated and the heat accumulated in commercially available Lithium-ion cells using an accelerated calorimeter along with a battery cycler and precision multi-meter. An integral energy balance was used to determine the total heat generated in the test cell during cycling. From the measurements during temperature transients, the heat capacity of the test cell was found to be relatively independent of temperature. This values agrees relatively well with separate measurements using an adiabatic calorimeter which yield slightly higher values. The reversible heat effect derived from an energy balance was found to be exothermic during discharge and endothermic during charge. Using two different methods, potentiometric method and energy balance method, values were obtained for entropy of reaction during discharge of the cell and results showed a weak dependence entropic heat on temperature. A strong rate dependent exothermic heat effect was

detected during discharge and endothermic effect occurs during early stages of charge, followed by a weaker exothermic effect.

Viswanathan, et al. [32] measured the entropy changes in various individual cathode and anode materials, as well as in full cells, using an electrochemical thermodynamic measurement system (ETMS). $LiCoO_2$ is found to have a larger entropy change compared to other cathodes. The reversible heat generation rate was found to have significant contribution of 700% of irreversible heat for $LiCoO_2$ based cells at C/8 rate in the 5-40% SOC range, while the contribution from $LiFePO_4$-LTO cells is 30% of irreversible heat.

Zhang, et al. [83] studied the charge and discharge characteristics of commercial $LiCoO_2$-based 18650 cells by using various electrochemical methods. Ragone plots [84] show that the effect of discharge power on the energy is significantly increased with decrease in the temperature. The combined benefit of the high power and energy densities can be optimal only at temperatures of 20°C or above. Poor performance at lower temperatures is due to high charge transfer resistance (R_{ct}). The R_{ct} has strong dependence on the cell's DOD and is much more sensitive to temperature change than the R_b and R_{SEI}.

Srinivasan and Wang [85] analyzed the thermal behavior of Li-ion cells by using a 2-D thermal-electrochemical model, by incorporating various sources of heat and the temperature dependence of the various parameters based on Arrhenius expressions. Model simulations were first used to show the 2D effects that can occur in cells with a large aspect ratio, under certain conditions. The contribution of various sources of heat at different operational rates is determined. Model simulations, used to estimate the thermal and electrical energy and the utilization of the cell at various rates, were used to gain insight into the effect of the electrochemistry on the heat-generation and vice versa. The model was also used to test

the hypothesis of using experimental voltage or calorimetric data to estimate the heat generation under one thermal environment, which is then used to predict heat generation under other environments. The use of voltage data to estimate heat generation was shown to be less rigorous compared to measuring this quantity directly from calorimetric data. However, this approach need to be used with caution as the heat generation measured under one thermal environment cannot be used under any other conditions.

Shah, et al. [81] presented an analytical model based on time dependent heat generation rate to predict the transient temperature field in a cylindrical Li-ion cell with an anisotropic thermal conduction within the cell. Experimental measurements from a thermal test cell are used to verify the model.

Kim, et al. [86] reproduced the 1D model formulated by Hatchard, et al. [33] and then extended it to three dimensions to include geometrical features, which are critical in large cells, to further understand the thermal behavior of large format Li-ion batteries. The three-dimensional model is used to simulate the oven tests to determine the propagation of local hot spots in the cell. The model shows that under identical abuse conditions, the smaller cell rejects heat faster than the larger cell. Initially the reactions propagate in the azimuthal and longitudinal directions to form a hollow cylinder-shaped reaction zone, then spread to center core and finally propagates to the outer rim of the cell.

Al Hallaj and Selman [56] proposed and investigated a novel thermal-management system that incorporates phase-change material (PCM). A commercial finite-element (FE) software, PDEase2D™, was used to simulate the thermal behavior of EV battery modules with a PCM thermal management system. Simulation results show that the temperature profile of the cells integrated in the module design was substantially more uniform during discharge at

different rates than without PCM. The PCM system is effective in thermally sensitive batteries such as Li-ion and most Li-polymer batteries with a significant reversible heat effect. The heat generated during discharge and stored as latent heat is then largely utilized during charge, and a smaller part of it is transferred to the surroundings. The stored heat will be rejected to the module when the battery is left to relax or when its temperature drops below the melting point of the PCM. This is an important advantage for EV operation under cold conditions or in space applications where the battery temperature drops significantly when an orbiting satellite moves from the light to the dark side of the earth.

Pesaran [87] reviewed some of the problems and solutions associated with proper design of the battery thermal management systems. Thermal management of batteries has become important in both EVs and HEVs for effective operation in all climates. There are trade-offs between performance, functionality, volume, mass, cost, maintenance, and safety but a proper thermal management system should have a positive impact on overall pack. A thermal management system using air is less complicated, though less effective, than a system using liquid cooling/heating. The location of the battery pack has a strong impact on the overall battery thermal management.

Chen, et al. [12] developed a 3-D model, considering the layered-structure of the cell stacks, the case of a battery pack, and the gap between the both elements, to examine the thermal behavior of a Lithium-ion battery. Spatial dependent convective and radiation boundary conditions are implemented. A simplified thermal model is proposed with various simplifications and validated with the detailed thermal model and found to be faster with an error less than 0.54 K.

Thermal management systems needs to be properly designed to have the operating temperature of batteries in within a narrow optimal range. Wang, et al. [88] explored the thermal performance of various battery module arrangements. The effect of location of cooling fan on the temperature uniformity, cooling capability was analyzed.

Thermal management system is of critical importance for a Li-ion battery pack, as high performance and long battery pack life can be simultaneously achieved when operated within a narrow range of temperature around the room temperature. An efficient thermal management system is required to keep the battery temperature in this range, despite widely varying operating conditions. Basu, et al. [89] introduced a novel liquid coolant based thermal management system, for 18,650 battery pack, which is designed to be compact and economical without compromising safety and constructed a coupled three-dimensional electrochemical model for the proposed pack. The model is used to evaluate the effects of different operating conditions like coolant flow-rate and discharge current on the pack temperature. Contact resistance is found to have the strongest impact on the thermal performance of the pack. From the numerical solution, a simple and novel temperature correlation of predicting the temperatures of all the individual cells given the temperature measurement of one cell is devised and validated with experimental results. Such coefficients have great potential of reducing the sensor requirement and complexity in a large Li-ion battery pack, typical of an electric vehicle.

Sun, et al. [90] developed a three-dimensional to simulate the thermal behavior of battery cells in a pack which incorporates a 3-D CFD pack-level sub-model, a 1-D battery pack network sub-model, and a 3-D thermal-electrochemical coupled cell/module level sub-model to predict the non-uniform heat generation rate, temperature distribution in the battery and the

temperature variation across the pack. It is verified with physical tests and a good correlation is found.

Fan, et al. [91] performed three-dimensional transient thermal analyses of an air-cooled module with air cooling through evenly-spaced channels on both sides of each cell and found that lowering the gap spacing and/or increasing flow rate of the fan lead to a decrease of the maximum temperature rise. Analyzing numerous designs, it is concluded that the temperature gradients along the air flow direction can be affected but cannot be avoided.

Guo and White [92] proposed a numerical method that can be used to reduce the computational difficulties in modeling the electrical and thermal behavior of a spirally wound cylindrical Li-ion cell. By analyzing the winding locus of the electrodes, some important geometric relationships of the spiral surfaces are identified, and algorithms for coordinate transform and variable extrusion between 2-D and 3-D domains are derived. The accuracy of variable extrusion could be improved by using more effective approximation approaches to express variables as explicit functions of 2-D coordinates. This numerical method enables the jellyroll model to be solved without using extremely fine mesh and thus greatly lowers the memory requirements saves computation time.

Zhao, et al. [93] developed a flexible hydrogen-based BTMS based on cost effective sodium-polyacrylate and can be arbitrarily shaped and conveniently packed to accommodate any Li-ion stacks. This BTMS is tested through a series of high-intensity discharge and abnormal heat release processes, and its performance is compared with three classical BTMS. The test results demonstrate that the proposed low-cost, space-saving, and contour-adaptable BTMS is a very economic and efficient approach in handling the thermal surge of Li-ion batteries. Based on the high moisture content, the hydrogel based BTMS keeps the most

advantages of water (i.e., high specific heat capacity and medium heat conductivity) and in the meantime, the mobility of water is prevented. In discharge tests, the proposed hydrogel BTMS shows its effectiveness in dissipating the generated heat from the battery packs without requiring an additional power supply. The advantage of hydrogel BTMS in dealing with extreme conditions is also tested through a series of nail penetration tests. Relying on its high resistance, high viscosity and high specific heat capacity, the proposed hydrogel based BTMS can either extend the safety time or prevent the occurrence of thermal runaway, and the voltages of the battery cells after the penetration testing can remain at a high level. The proposed hydrogel based BTMS is targeted to stationary or mobile battery packs that require a compact, accessible, and power-saving cooling system to suppress the unexpected thermal surge or runaway under normal and extreme conditions. This BTMS can be implemented in an open or a closed structure to address the problems associated with evaporation, humidity and volume change during phase change, and the packaging of the proposed cooling system can be customized based on the size and shape of the electric device.

Zhao, et al. [94] established numerical simulation for air cooling in battery models for cylindrical Lithium-ion battery pack and carried a detailed parametric investigation to study effects of parameters on the performance of thermal management of the battery pack.

He and Ma [95] studied the problems associated with thermal management systems of batteries under extreme hot conditions. Due to the difficulty of conducting experiments under extreme conditions, they first conducted controlled experiments to validate their CFD models then the CFD models were used to study the various issues of thermal management systems in batteries. The design and optimization involves a trade-off between several aspects and the

results obtained illustrate both the conflicting nature of these aspects and an improved design obtained when all these aspects are balanced properly.

Song, et al. [96] established an electrochemical–thermal coupling model based on the finite element method to simulate the thermal behavior of $LiFePO_4$ Lithium ion battery during charge–discharge process, and the effect of operational rate and ambient temperature. The heat generation rate in the battery increases as charge–discharge proceeds. At high rates, the irreversible heat is the major contributor while at low rates, reversible heat dominates. Effect of the ambient temperature on the cell temperature is found to be significant.

Daud, et al. [97] presented and validated an electro-thermal model for Lithium ion batteries in automotive applications, which is implemented in OpenFOAM software to link the thermal losses inside battery cells to radiation and forced convection. Heat sources are assumed to be present at the connectors and are calculated as a function of battery discharge current and internal resistance and simulation results are validated against experimental results.

Most of the thermal models and coupled electro-chemical models developed today are mathematical models based solely on theoretical analysis. Though, using this models, we can analyze numerous cases which otherwise might not be possible by using experiment models, they have many assumptions and approximations and may not be accurate since they do not consider a lot many things that might come into play while the battery is operated in real case scenarios. By using experimental models, we can have data on the cell which is more closely related to the battery operating practical conditions. And, theoretical models need to be validated by experimental data. Coming to the experimental models existing, they generally use accelerated rate calorimetry (ARC) for their experiments. Calorimeter provides an adiabatic environment when it detects an exothermic reaction and collects temperature,

pressure and time data during the entire process and generates the heat generation rates. The cost involved with this equipment is too high, so it is limited to very few highly funded laboratories. Even in such labs, the experiment cost involved limits the number of experiments that could be done or number of times an experiment can be repeated. Also, since we cannot carry this equipment to wherever necessary, the experiments must be done only in those laboratories, rendering the ability to carry in situ experiments. Also, the limited access of this equipment to a very few laboratories limits the amount of research that could be done into thermal analysis of Lithium ion batteries experimentally.

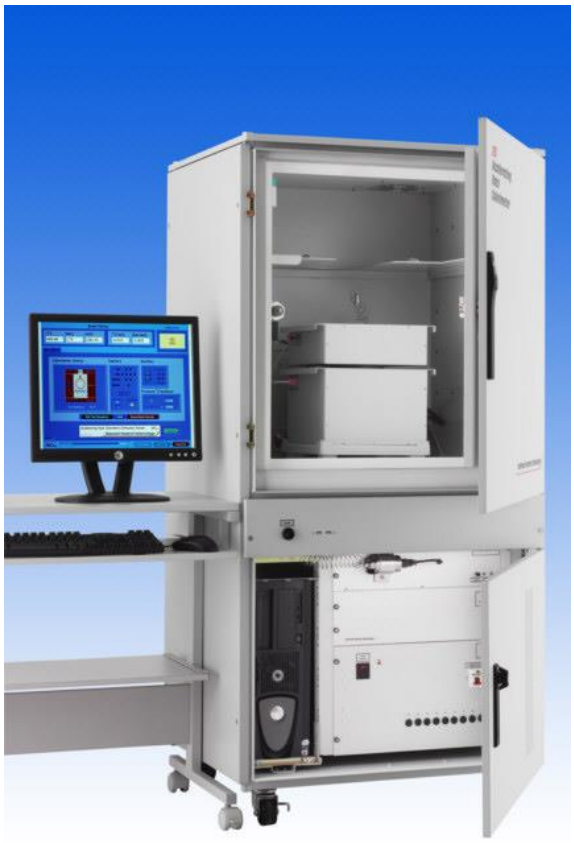

Figure 9. Accelerating rate calorimeter (ARC) [98].

There are very few experiments done to quantify the amount of heat generation in cylindrical cells with NMC and graphite as cathode and anode respectively. Zhang, et al. [99] designed and manufactured 18650 Li-ion cells with $LiNi_{1/3}Co_{1/3}Mn_{1/3}O_2$ (NCM) and graphite as positive and negative electrode materials, respectively and with multiple micro thermocouples embedded inside their jelly rolls. Arbin BT2000 cycler is used to control the overall current/ voltage of the experimental cell and T-type micro thermocouples are used for measurement of internal temperatures. Temperatures distributions along the radial direction of these cells are obtained and effects of various important operating parameters, including discharge C-rate, ambient temperature and cooling condition on the temperature distribution are investigated. Correlation between relative temperature gradient in radial direction and cooling coefficient is investigated which indicate that the assumption of uniform temperature distribution is applicable under natural cooling conditions but not applicable under strong forced convection cooling conditions.

Ji, et al. [100] developed an electrochemical-thermal coupled model, incorporating concentration and temperature dependent transport properties and is validated against 2.2 Ah 18650 cylindrical cells with $LiNi_{1/3}Co_{1/3}Mn_{1/3}O_2$ (NCM) and graphite as positive and negative electrode materials respectively, over a wide range of temperatures and discharge rates. Simulation and experimental results demonstrate the dramatic effects of cell self-heating upon electrochemical performance.

Chacko and Chung [61] developed the fully coupled, three-dimensional transient electro-thermal model for time-dependent, thermal behavior of a Li-ion polymer cell based on finite volume method. The model is validated by testing a high-energy density Li-ion polymer pouch cell, with graphite anode and $LiNi_{1/3}Co_{1/3}Mn_{1/3}O_2$ (NCM) cathode with nominal

capacity of 20 Ah, in a climatic chamber for electric load cycles consisting of various charge and discharge rates.

A robust, calorimeter-free experimental method to quantify the total amount of heat generated in an 18650 cylindrical Li-ion cell is presented in this work. The method uses inverse heat-transfer analysis to quantify the total amount of heat generated in the cell from the surface temperature measurements of the cell during an electro-chemical operation of the cell. The model does not consider any of the individual electrochemical reactions taking place in the cell. It considers only the net heat generated in the cell, which is the result of all the electrochemical reactions occurring, thermo-physical properties of all the cell components. The model predicts the amount of heat generated in the cell by measuring the surface temperature of the cell which is the resultant of the amount of heat generated in the cell and amount of heat transferred from the cell to the surroundings. After quantifying the total heat generation, the contribution of individual sources of heat generation is quantified. The total heat generated in the cell is assumed to be only due to the irreversible joule heat and reversible entropic heat.

CHAPTER III

CALORIMETER FREE HEAT QUANTIFICATION

Methodology

Experimental setup

The commercially available Panasonic CGR18650CG cylindrical Li-ion battery with 2250 mAh capacity is used for testing. The cell is connected to arbin BT2000 battery cycler and Type-K thermocouple is attached to the surface of the cell using thermal conducting tape which is used for collecting cell surface temperature measurements and is connected to the auxiliary system of the arbin. This entire setup is placed in a space which is closed as shown in Figure 10, to prevent sudden fluctuations in temperature and maintain near constant ambient room temperature.

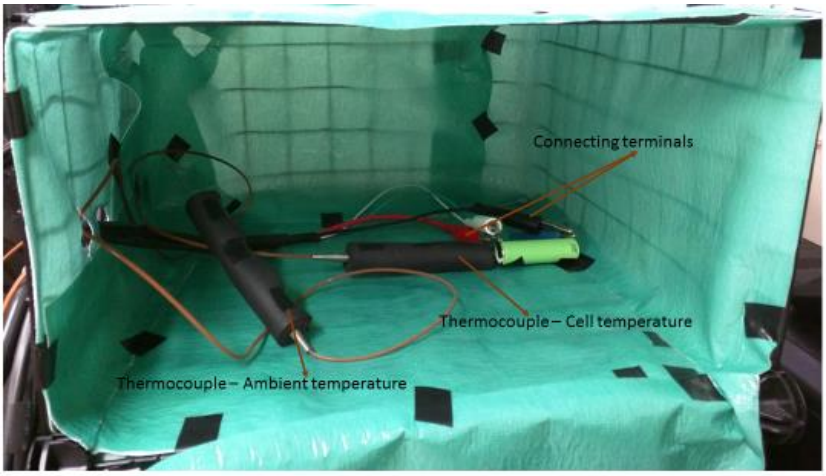

Figure 10. Experimental setup of Panasonic CGR18650CG battery.

MSDS of the cell

- Positive electrode – Lithium nickel manganese cobalt oxide (NMC), 20-35wt%
- Negative electrode – Carbon, 10-20wt%

- Enclosure – Plastic
- Safe voltage limits: 2.8 V ~ 4.2 V

Table 1. MSDS of the CGR18650CG cell

Nominal voltage		**3.6 V**
Standard capacity		2250 mAh
Dimensions	Diameter	18.6+0/-0.7 mm
	Height	65.2+0/-1.0 mm
	Weight	Approx. 45 g

Protocol

Initially, a fresh 18650 cell is taken and formation cycles are done on it using the following protocol

a. Charge the cell at C/20 cycling rate till it reaches upper cut-off voltage, 4.2 V.
b. Rest the cell for one hour.
c. Discharge the cell at C/20 cycling rate till it reaches lower cut-off voltage of 2.8 V
d. Rest the cell for one hour.
e. And repeat the steps a to d for two times.

After formation cycles, the cell is cycled using the following constant current "rest-charge-rest-discharge" protocol.

a. Allow the cell to rest for one hour after formation cycles.
b. Then charge the cell at constant current (CC) corresponding to one of the C-rate: C/5, C/2, 1C, 2C, 3C, 4C with upper cut-off voltage as 4.2V.

c. Rest the cell for 2 hours after charge.

d. Now discharge the cell at constant current (CC) corresponding to one of the C-rate: C/5, C/2, 1C, 2C, 3C, 4C with lower cut-off voltage as 2.8V.

e. Rest the cell for 2 hours after discharge.

f. Repeat the steps g to j for 10 charge-discharge cycles for each of the C-rate: C/5, C/2, 1C, 2C, 3C, 4C, with the same voltage window of 2.8V ~ 4.2V.

Thermal modeling and analysis

The thermal response (i.e. temperature rise) is a function of thermo-physical properties of battery as well as electrochemical operation. Mathematically these various aspects are strongly coupled and governed by

a. Mass/species balance

b. Charge balance

c. First law of thermodynamics

Batteries being composed of a complex electrode microstructure and multiple material phases, accurate quantification of every parameter and material property become cumbersome. Thence, if possible an alternate simplified strategy should be developed to quantify heat generation rates as a function of electrochemical operation. This technique has quite many assumptions and should be used with care.

1. 18650 cells have small enough thermal mass and large enough thermal conductivity for them to be represented by a single temperature by lumped capacitance model. This can also be quantified by using dimensionless quantity, Biot number (Bi), which is the ratio of internal conductive resistance over surface convective resistance

$$Bi = \frac{hL}{k} = 0.015 \ll 0.1$$

Taking effective thermal conductivity (k) for 18650 cell as 3 W/m-K; convective heat transfer coefficient (h) as 10 W/m^2-K for air and L=Volume of cell/Area of cell (where volume = $\frac{\pi D^2 H}{4}$, area = πDH, diameter of cell (D) =18.6 mm, height (H) =65.2 mm), Bi number is 0.015, so lumped heat capacitance model is valid.

2. The surface temperature of the cell is a resultant of the total heat generated in the cell and the total amount of heat transferred to the surroundings.
3. The heat transferred from the cell to the surroundings is assumed to be only by convection heat transfer.

With all these assumptions, starting from an energy balance in the cell, the thermal balance equation can be given by

Equation 1: $$\boldsymbol{mC_P \frac{dT}{dt} = -hA(T_{cell} - T_\infty) + \dot{Q}_{gen}}$$

Where m is the mass of the cell (0.044 kg); C_P is the heat capacity of the cell $\left(840\ \frac{J}{kg-K}\right)$; h is convective heat transfer coefficient; A is the area of cell exposed to environment (0.0044 m^2); T_{cell} is the temperature of the cell; T_∞ is the ambient temperature (T_{amb}); $\dot{Q}_{gen}$ is the total heat generation in the cell ($\dot{Q}_{gen} = \dot{q}_{gen} V$, where $\dot{q}_{gen}$ is volumetric heat generation rate; V is the volume of the cell (0.17716e-04 m^3).

Since the surface temperature of the cell, ambient temperature, current and voltage during charge and discharge are measured using arbin system and as we already know the mass, specific heat capacity and area of the cell, the only unknowns left in Equation 1 are

a. Total heat generation rate ($\dot{Q}_{gen}$) and
b. Film coefficient for convection from cell surface (h)

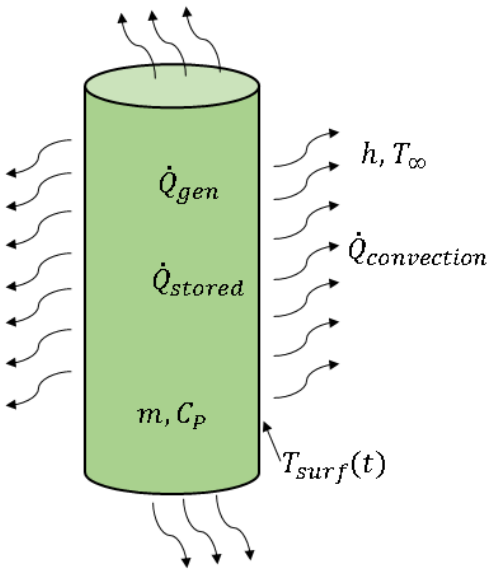

Figure 11. Schematic of energy balance in a cell with necessary assumptions.

During any electrochemical operation both the terms on the right-hand side are active. But if we consider enthalpy of mixing to be small, there is no heat generation during rest period of the cell. This fact can be used to back compute heat transfer coefficient, h, from the temperature data available during rest period. Then heat generation rate, $\dot{Q}_{gen}$, can be quantified by from temperature data during charging and discharging combined with heat transfer coefficient value obtained from data during rest period. This process can be represented using the following Figure 12 and Figure 13.

i) During rest period, the schematic of energy balance is as shown in Figure 12.

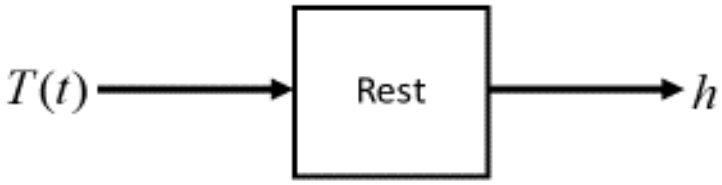

Figure 12. Schematic of analysis on cell during rest period.

ii) And during charging and discharging operation, the schematic of energy balance is given as shown in Figure 13.

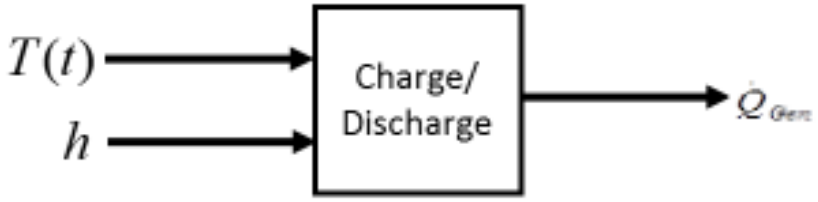

Figure 13. Schematic of analysis on the cell during charge/discharge operation.

The corresponding governing equation for rest period after analyzing Equation 1 is given by

Equation 2: $$\boldsymbol{mC_P\frac{dT}{dt} = -hA(T_{cell}(t) - T_\infty)}$$

Or,

$$\frac{dT}{dt} = -\frac{1}{\tau}(T_{cell}(t) - T_\infty)$$

Where, time constant $(\tau) = \frac{mC_P}{hA}$;

Assuming the ambient temperature to be a constant and integrating Equation 2 by applying the limits on cell temperature and time, we arrive as follow:

$$\int_{T_0}^{T} \frac{dT}{T_{cell}(t) - T_\infty} = -\int_0^t \frac{dt}{\tau}$$

$$\ln(T_{cell}(t) - T_\infty)|_{T_0}^{T} = -\frac{t}{\tau}\Big|_0^t$$

Equation 3: $$\boldsymbol{\ln\left(\frac{T_{cell}(t) - T_\infty}{T_0 - T_\infty}\right) = -\frac{t}{\tau}}$$

Or,

$$(T_{cell}(t) - T_\infty) = (T_0 - T_\infty)\exp\left(-\frac{t}{\tau}\right)$$

From the experimental data, the values of $T_{cell}(t)$, T_∞ and t are available which reduces finding of τ to a curve fitting problem. Fitting the given data set using non-linear least square regression method by rearranging Equation 3 to the following form

Equation 4: $$\boldsymbol{y = f(x, \alpha) + \beta}$$

Where, $y = T_{cell}(t)$, $f(x, \alpha) = (T_0 - T_\infty) \exp\left(-\frac{t}{\tau}\right)$ and $\beta = T_\infty$, we can get τ value that best fits the data, which can later be used to quantify the total amount of heat generation.

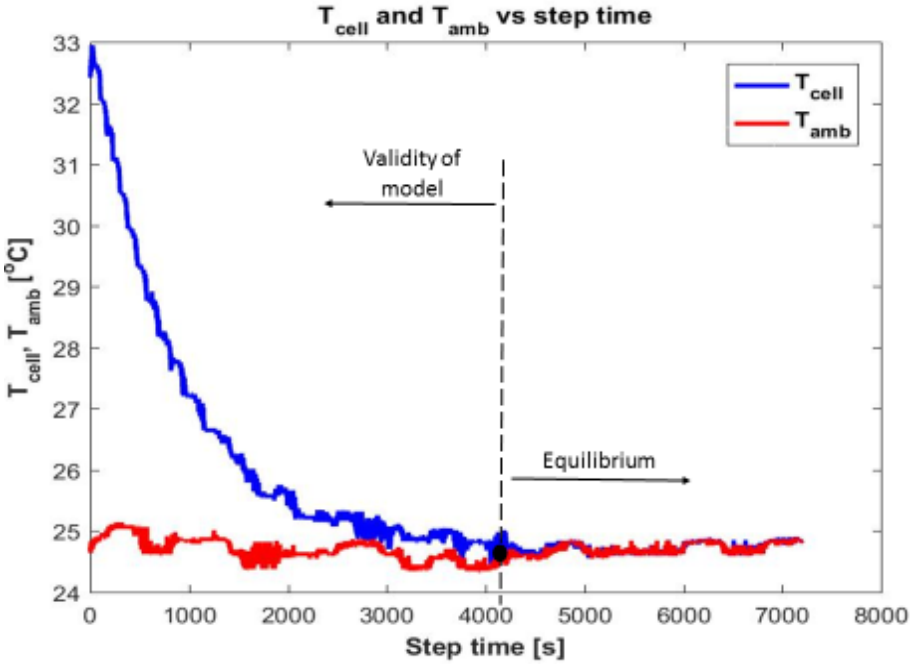

Figure 14. T_{cell}, T_∞ vs. time during the rest period for the cell cycling at 1C-rate.

This whole formulation is based on assumption of constant ambient temperature which might be difficult in practice without using a sophisticated closed loop control system. But the formulation can be still applied if the changes in the value of $T_{cell}(t)$ are about an order of magnitude greater than the fluctuations in T_∞. Graphically this zone is determined

by simultaneously plotting $T_{cell}(t)$ and T_{∞}. Once thermal equilibrium is established, changes in $T_{cell}(t)$ quite closely follow that in T_{∞} as shown in Figure 14. Once the curve that best fits the temperature and time data by using Equation 4 is obtained, the goodness of the fit can be determined by calculating R-squared value as shown in Table 2.

Table 2. Calculating R-squared value to determine the goodness of fit

a. Mean temperature, $T_{mean} = \frac{1}{n}\sum_{i=1}^{n} T_{cell}(i)$,

b. Total sum of squares, $SS_{tot} = \sum_{i=1}^{n}(T_{cell}(i) - T_{mean})^2$,

c. Residual sum of squares, $SS_{res} = \sum_{i=1}^{n}\left(T_{cell}(i) - T_{fit}(i)\right)^2$

And R-squared value, $R^2 = 1 - \frac{SS_{res}}{SS_{tot}}$

Where n is total number of data points during the test and T_{fit} is the fitted temperature data.

Results and discussions

The following plots from Figure 2 to Figure 13 shows the experimental and correlated temperature data during rest after charge and rest after discharge of the cell at various C-rates: C/5 to 4C with R^2 value representing the goodness of correlation.

From Figure 15 to Figure 20, we can see the goodness of fit for all the curves is pretty much high, greater than 90%, which indicates that fitted data closely represents all the variations that exists in the original data and visual inspection of plots shows that the fitted curves are valid. After τ values are obtained from fitting the temperature and time data

collected during the operation of the cell with Equation 4, the convective heat transfer coefficient values (h) are calculated by using the following relation:

$$\tau = \frac{mC_p}{hA}$$

The convective heat transfer coefficient values calculated are averaged over 10 cycles for each of the C-rate and are as shown in Table 3.

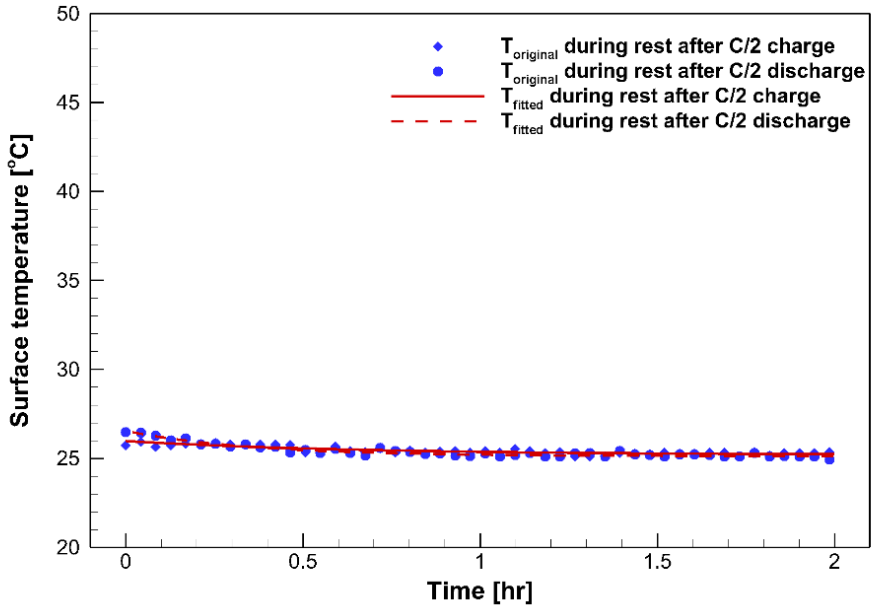

Figure 15. Surface temperature of the cell vs. time during rest after charge and discharge at C/2-rate.

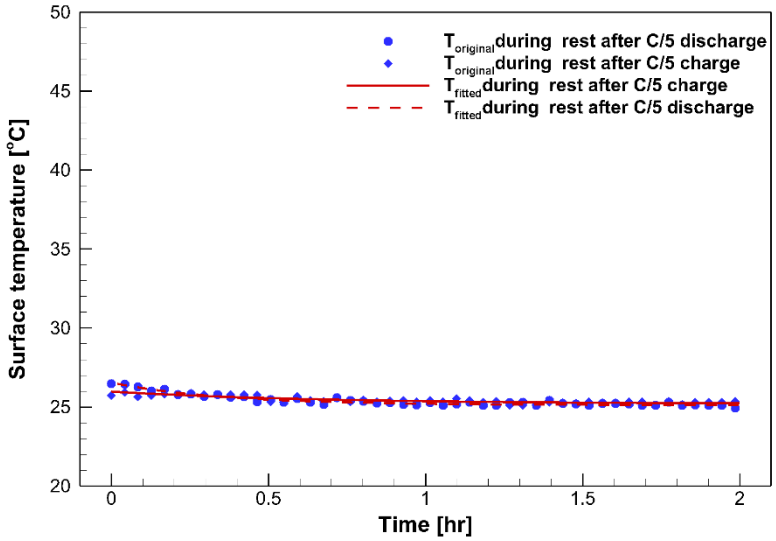

Figure 16. Surface temperature of the cell vs. time during rest after charge and discharge at C/5-rate.

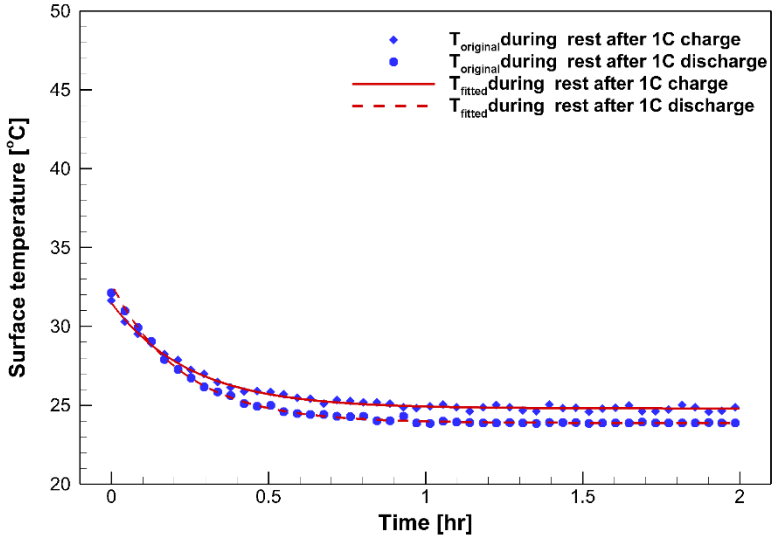

Figure 17. Surface temperature of the cell vs. time during rest after charge and discharge at 1C-rate.

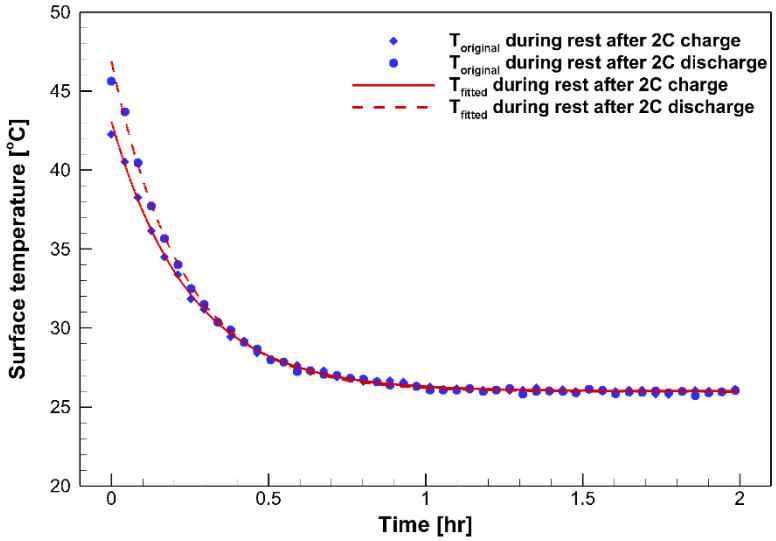

Figure 18. Surface temperature of the cell vs. time during rest after charge and discharge at 2C-rate.

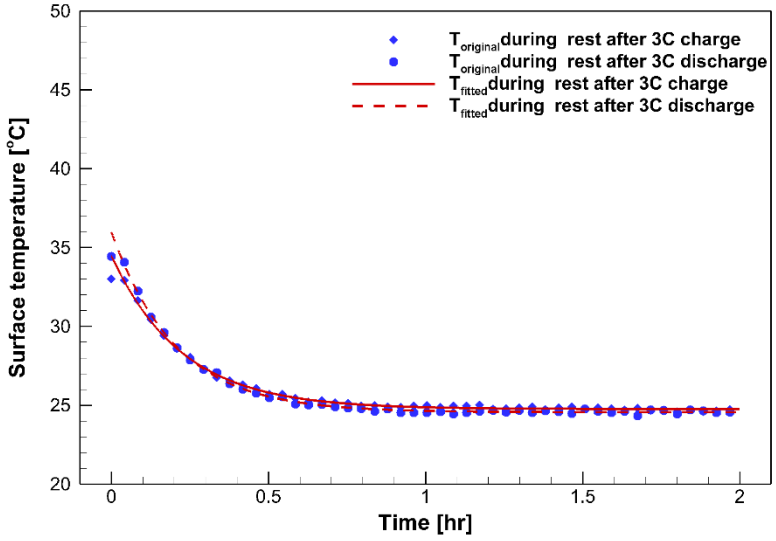

Figure 19. Surface temperature of the cell vs. time during rest after charge and discharge at 3C-rate.

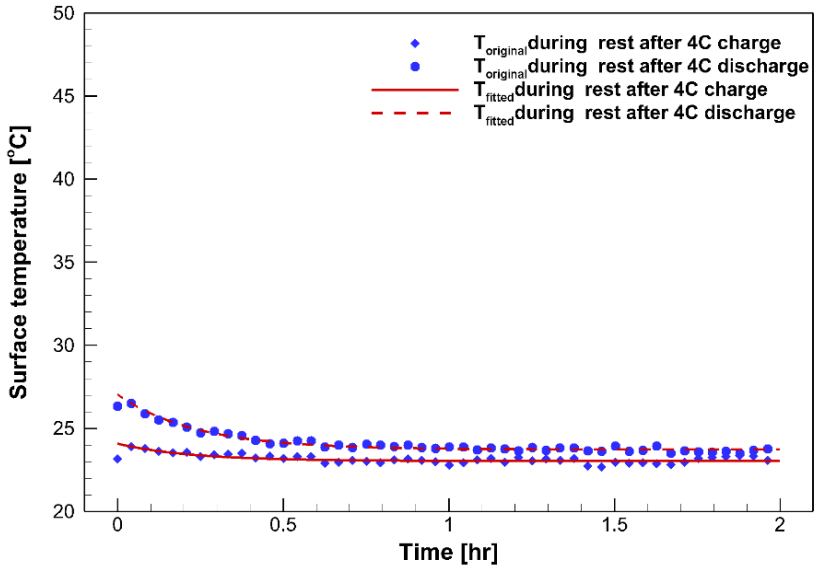

Figure 20. Surface temperature of the cell vs. time during rest after charge and discharge at 4C-rate.

Table 3. Average convective heat transfer coefficient values for various C-rates.

C-rate	Average heat transfer coefficient values (W/m^2K)	
	Rest after charging	Rest after discharging
C/5	6.986	6.556
C/2	9.672	8.770
1C	10.308	9.416
2C	10.323	9.355
3C	11.248	10.078
4C	9.891	13.126

Voltage profiles

The voltage profiles shown in Figure 21 clearly indicate that the both charge and discharge capacities decreases as we go for the higher C-rates. The decrease in voltage at the start of both charging and discharging is slightly steeper and by the end of discharge the decrease is very steep.

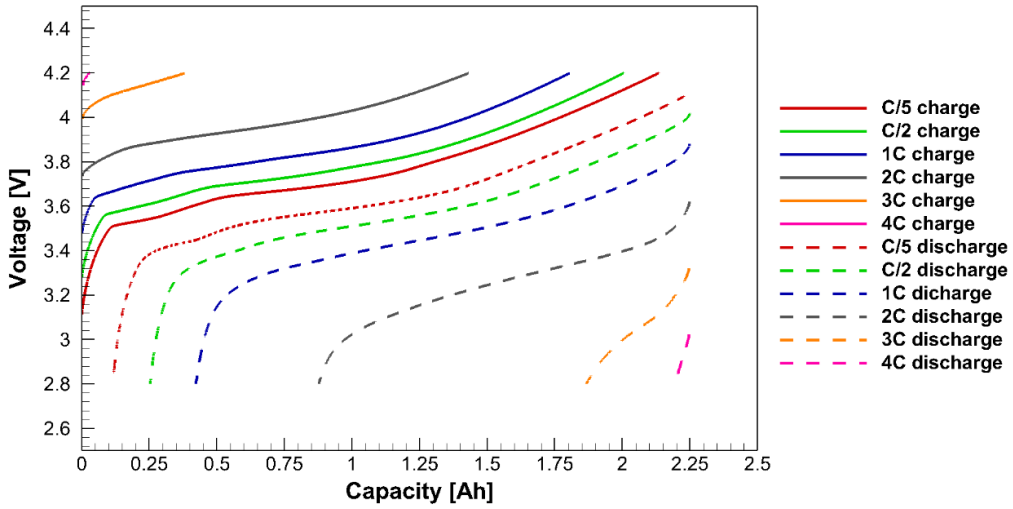

Figure 21. Voltage profiles during the charging and discharging of the cell at various C-rates.

Quantification of total heat generation

Unlike during resting period, there will be internal heat generation $\dot{Q}_{gen}$ during charging and discharging of the cell, which is a function of state of charge (SOC) and C-rate. Once heat transfer coefficient values (h) are obtained, this total heat generation rate ($\dot{Q}_{gen}$) can be quantified by fitting the data collected during charging and discharging operation of the cell by simultaneously using the h values calculated for respective C-rate and the fitting Equation 5. By using the lumped capacitance model and applying energy balance over CGR18650CG

cell during an electrochemical operation, the governing differential equation obtained is given by Equation 1 as follows:

$$\dot{Q}_{gen} - hA(T_{cell} - T_{\infty}) = mC_P \frac{dT}{dt}$$

Where T in $\frac{dT}{dt}$ corresponds to cell temperature $T_{cell}(t)$. By rearranging this equation,

Equation 5: $$\boldsymbol{\dot{Q}_{gen} = mC_p \left(\frac{dT_{cell}(t)}{dt} + \frac{T_{cell}(t) - T_{\infty}}{\tau_{max}}\right)}$$

Where $\tau_{max} = \frac{mC_p}{hA}$. Here $\tau_{\max}$ is the time constant, which is the time by which the cell reaches the 63.21% of the total increase in temperature during the charging sequence considered.

Given $T_{cell}(t)$, it will be to obtain $\dot{Q}_{gen} = Q(t, I) = Q(SOC, C - rate)$. To do that, it is necessary to accurately quantify the slope, $\frac{dT_{cell}(t)}{dt}$, which will be used in the governing differential Equation 5. A typical temperature profile of an 18650-cell obtained during the charging operation is as shown in Figure 22. The temperature of the cell increases with time during charging due to the internal heat generation, mainly contributed by

a. Joule heating due to internal resistances and

b. Entropic or reaction heat due to entropy changes.

It is clear from Figure 22, the experimental data contains noise (jagged) features. Hence the computation for $\frac{dT_{cell}(t)}{dt}$ must be insensitive to random noise. This rules out typical numerical differentiation. The plot in Figure 22 is quite like that of $y = 1 - e^{-x}$, hence exponential correlation function is a natural choice and let the fitting function be

Equation 6: $$\boldsymbol{T_{cell}(t) = \left(\sum_{j=1}^{N} c_j e^{-\frac{t}{\tau_j}}\right) + c_{N+1}}$$

As such, it is a non-linear regression problem, but if time constant τ_j is known, it converts to a linear regression problem. Time constants lie between τ_{min} and τ_{max}. Here minimum time constant $\tau_{min} = \frac{2}{f_{sampling}}$, while maximum time constant, τ_{max} can be taken as system's characteristic time ($i.e. \tau_{max} = \frac{mc_P}{hA}$) and other time constants are geometrically distributed between τ_{min} and τ_{max} i.e.,

$$\frac{\tau_{min}}{\tau_2} = \frac{\tau_2}{\tau_3} = \cdots = \frac{\tau_{N-1}}{\tau_{max}} = \frac{1}{r}$$

Once the coefficients of correlation are obtained, sufficient number of exponential terms (N) for the correlating equation is determined from goodness of correlation by calculating the R-squared value as shown in the Table 2. Sufficient number of exponential terms (N) for the correlating equation is found from R-squared value vs. no. of terms (N) plot (as shown in the Figure 23).

As shown in Figure 23, for charging at 1C data, R-squared value improvement is not much (it stayed same) after reaching number of exponential terms in the correlating equation to 15 and are as tabulated in Table 4, which are used for analysis. The correlation obtained by such analysis is as shown in Figure 24.

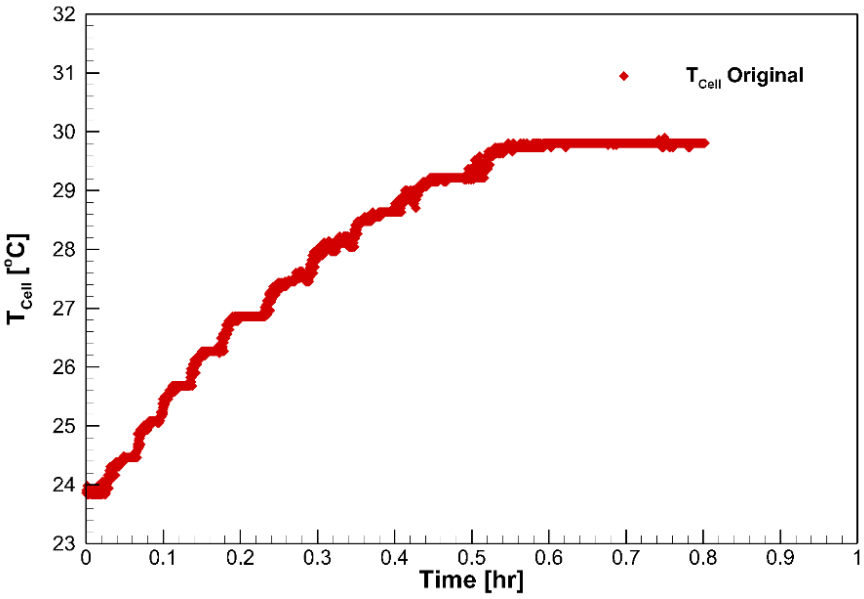

Figure 22. Temperature profile of an 18650 cell during the charging operation at 1C rate.

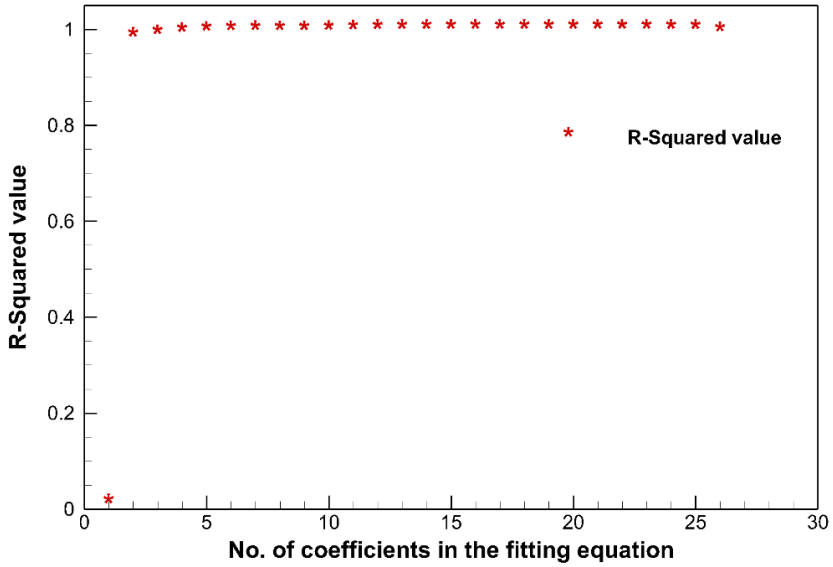

Figure 23. R-squared value vs. no. of terms in the correlating equation during the charging operation at 1C rate.

Table 4. Coefficients of all the terms used in analysis for charging at 1C-rate.

N^{th} term in equation	Coefficient value	N^{th} term in equation	Coefficient value
1	2.2007	9	409.1796
2	-12.9056	10	-393.9432
3	42.1846	11	402.0323
4	-100.2053	12	-408.3611
5	189.6467	13	347.7408
6	-295.6170	14	-197.6094
7	382.5609	15	45.9359
8	-418.1593	16	29.2308

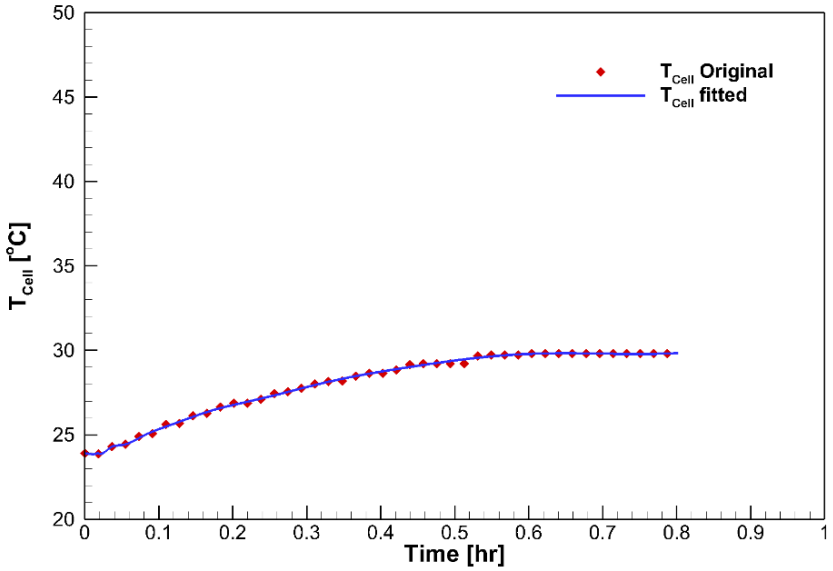

Figure 24. Fitted temperature and original temperature vs. time during the charging operation at 1C rate with R-squared value 0.9981.

Temperature profiles

Figure 25 shows us the correlated cell temperature (T_{fitted}) vs. capacity (in Ah) for various C-rates (C/2, 1C and 2C) during charging and discharging operation of the cell. From Figure 25, the temperature of the cell increases with time during both charging and discharging operations and this increment is more predominant as we go from lower C-rates to higher C-rates. The temperature of the cell during discharge is a little higher than during charging for a same C-rate. The temperature of the cell during charging increased initially, reaches maximum and then slightly decreased by the end of the charging. Whereas the temperature during discharging increased initially then decreased slightly and again increased towards the end of the discharge. The temperature of the cell during both charging and discharging increased more rapidly as we go for higher C-rates and maximum temperature in the cell increases with C-rate. The temperature of the cell at lower C-rate during charging/discharging remained almost constant (except for the small fluctuations which might be due to the fluctuations in ambient temperature) because the natural convection provided to the cell is sufficient to remove the small amounts of heat generated at such low rate of operation preventing the rise in cell temperature.

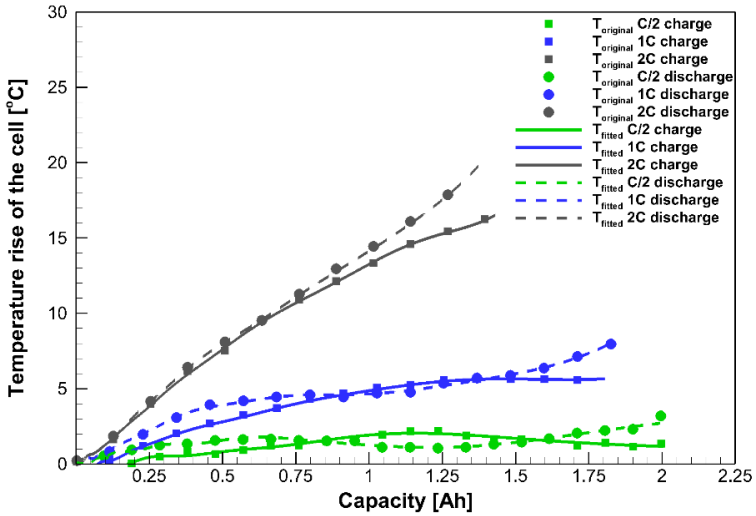

Figure 25. Correlated cell temperature (T_{fitted}) vs. capacity (Ah) for charging and discharging of the cell at various C-rates.

Total heat generation rates

The governing differential equation for heat generation previously obtained in Equation 5 is

$$\dot{Q}_{gen} = mC_p\left(\frac{dT_{cell}(t)}{dt} + \frac{T_{cell}(t) - T_\infty}{\tau_{max}}\right)$$

Where T_∞ is the average ambient temperature (same as $T_{amb} = 24.1870^oC$), $\tau_{max} = 850s$, $m = 44g = 44 * 10^{-3}kg$, $c_P = 830\,\frac{J}{kg-K}$ and using Equation 6, $\frac{dT}{dt} = -\sum_{j=1}^{N}\frac{C_j}{\tau_j}e^{-\frac{t}{\tau_j}}$.

After obtaining the necessary constants of fitting equation, $\frac{dT_{cell}(t)}{dt}$ can be calculated and then heat generation rate can be quantified. Figure 26 to Figure 29 shows the amount of heat generation rate in the cell with charge and discharge at various C-rates: C/2, 1C, 2C, and 3C. The rate of heat generation increases as we increase the rate of charge/discharge operation of the cell. The heat generation rate is slightly higher during discharge compared to charge for all C-rates. This is due to slightly endothermic effect of the reactions at cathode during

charging. The heat generation rate is more at the beginning of the charge and slightly increases to the middle of charge and decreases by the end of charge while the heat generation rate is more at the starting of discharge, decreases to the middle of discharge and increases by the end of the discharge. The higher heat generation at the beginning of charging and discharging is due to the large concentration gradients caused by the current while at the end of discharge it is due large ohmic drop and increased concentration potential. The rate of temperature change $\left(\frac{dT}{dt}\right)$ follows the same trend as the rate of heat generation. As we go for higher C-rates heat generations both during charging and discharging have almost similar trends

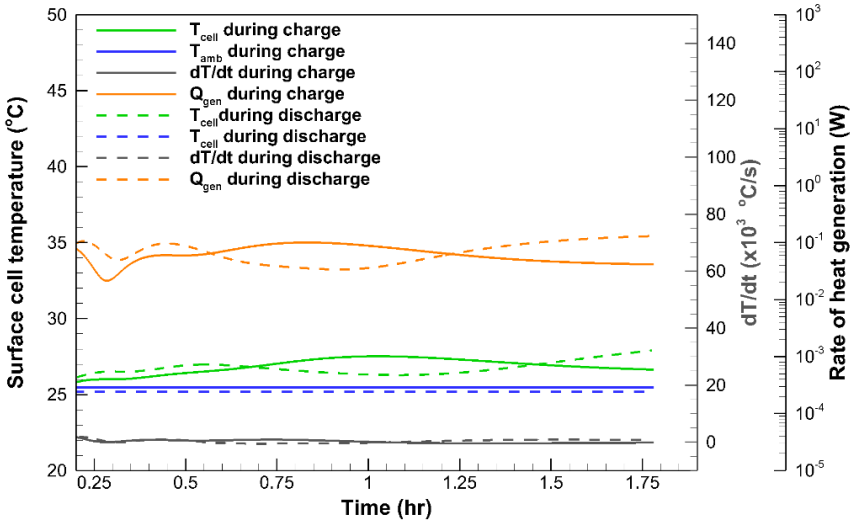

Figure 26. T_{cell}, $\frac{dT}{dt}$, rate of heat generation ($\dot{Q}_{gen}$) vs. time for charging and discharging at C/2-rate.

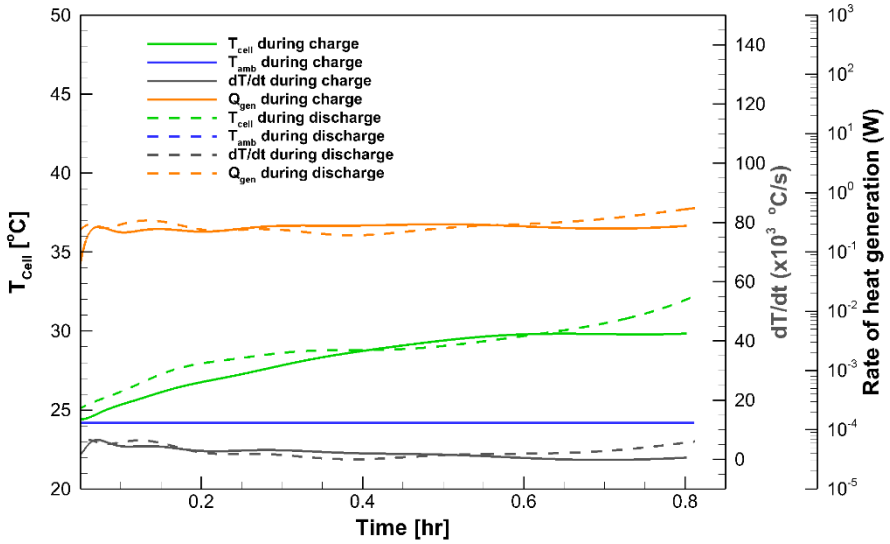

Figure 27. T_{cell}, $\frac{dT}{dt}$, rate of heat generation ($\dot{Q}_{gen}$) vs. time for charging and discharging at 1C-rate.

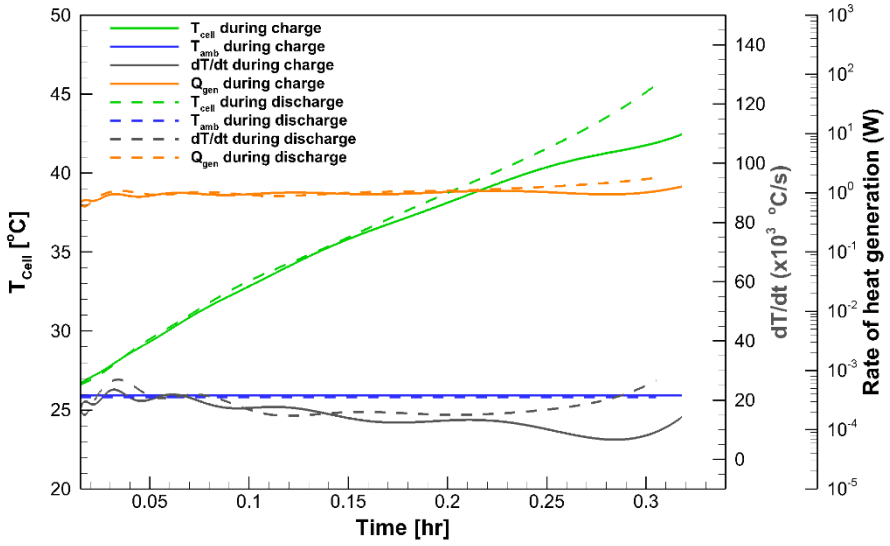

Figure 28. T_{cell}, $\frac{dT}{dt}$, rate of heat generation ($\dot{Q}_{gen}$) vs. time for charging and discharging at 2C-rate.

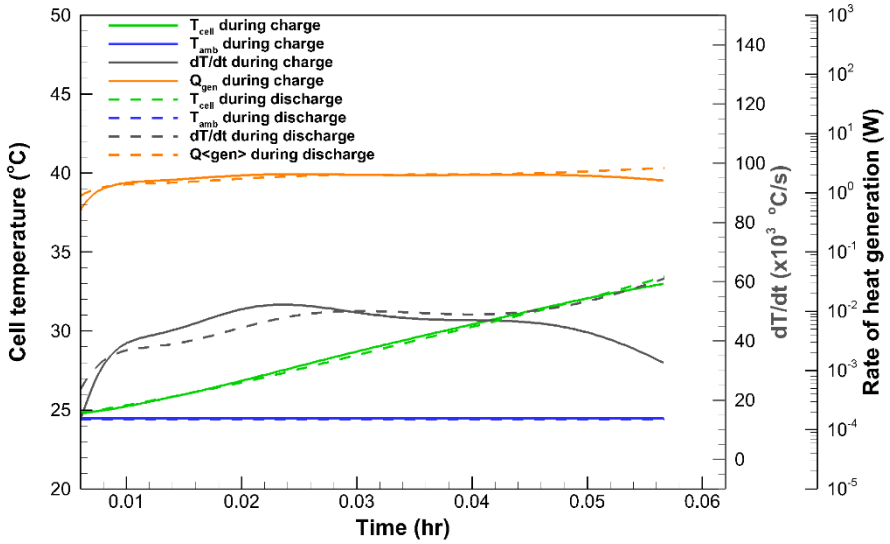

Figure 29. T_{cell}, $\frac{dT}{dt}$, rate of heat generation ($\dot{Q}_{gen}$) vs. time for charging and discharging at 3C-rate.

The average values of heat generation rate ($\dot{Q}_{gen}$) at various C-rates C/5, C/2, 1C, 2C, 3C during both charging and discharging are tabulated as shown in Table 5.

Table 5. Heat generation rate for charging and discharging at different C-rates.

C-rate	Average value of $\dot{Q}_{gen}$ during charging (W)	Average value of $\dot{Q}_{gen}$ during discharging (W)
C/5	0.0179	0.0125
C/2	0.0586	0.0754
1C	0.2480	0.2820
2C	0.9632	1.0483
3C	1.6188	1.7354

Figure 30 shows the experimental and correlated average total heat generation rates ($\dot{Q}_{gen}$) with varying C-rate: C/5, C/2, 1C, 2C and 3C rates during charging and discharging operation of the cell. The average heat generation rate ($\dot{Q}_{gen}$) data is correlated using following equations

a. For charging

$$f(x) = 0.0844x^2 + 0.3286x - 0.0977$$

b. For discharging

$$f(x) = 0.0794x^2 + 0.3860x - 0.1135$$

Where, $f(x)$ is the fitting function which gives heat generation rate values and x is the C-rate. The trends in heat generation rates calculated are like the trends followed by heat generation rates generated by Accelerated Rate Calorimetry (ARC) from the literature.

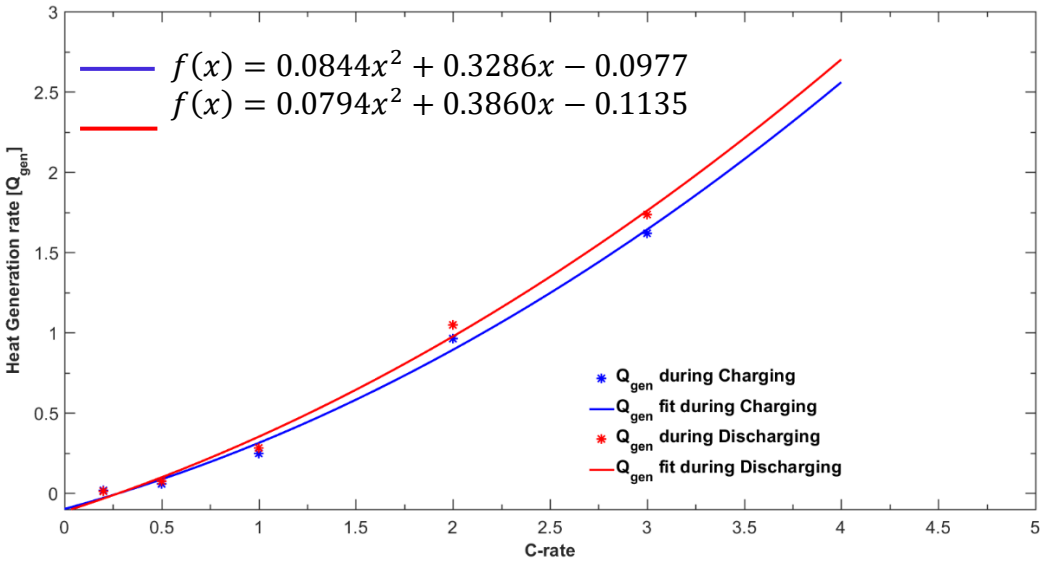

Figure 30. $\dot{Q}_{gen}$ vs. C-rate for original data and fit data during charging and discharging for various C-rates.

CHAPTER IV

QUANTIFYING SOURCES OF HEAT GENERATION

Sources of heat generation

Now as the total amount of heat generated in a cylindrical Li-ion cell can be quantified experimentally, it is essential to quantify the contribution of individual sources towards the total heat generation rate. The major sources of heat generation are assumed to be irreversible ohmic heat and reversible entropic heat. Heat generation rates due to concentration gradients are assumed to be negligible. So, the total heat generation is given by

Equation 7: $$\dot{\boldsymbol{Q}}_{\boldsymbol{gen}} = \dot{\boldsymbol{Q}}_{\boldsymbol{rev}} + \dot{\boldsymbol{Q}}_{\boldsymbol{irr}}$$

Where, $\dot{Q}_{rev}$ is the reversible heat generation and $\dot{Q}_{irr}$ is the irreversible heat generation. Irreversible heat generation ($\dot{Q}_{irr}$) is always exothermic and is given by

Equation 8: $$\dot{\boldsymbol{Q}}_{\boldsymbol{irr}} = \boldsymbol{I}(\boldsymbol{V} - \boldsymbol{U}) = \boldsymbol{I}^{\boldsymbol{2}}\boldsymbol{R}_{\boldsymbol{in}}$$

Where, I is the current in the cell which is negative during discharge and positive during discharge; V is cell potential, U is open circuit potential. Difference between V and U is the cell over-potential, $\eta_{cell} = (V - U)$ and is an indicative of irreversibilities such as ohmic losses in the cell, charge transfer over potentials at the interface and mass transfer limitations. The product of cell over potential (η_{cell}) and cell current (I) is known as polarization heat and is composed of joule heating within battery as well as the energy dissipated in electrode over potentials. And R_{in} is the internal resistance of the cell (Ω), which is the sum of ohmic, activation and diffusion polarization resistances and is given by cell over potential (η_{cell}) divided by cell current (I)

Equation 9: $$\boldsymbol{R}_{\boldsymbol{in}} = \frac{\boldsymbol{\eta}_{\boldsymbol{cell}}}{\boldsymbol{I}} = \frac{\boldsymbol{V}-\boldsymbol{U}}{\boldsymbol{I}}$$

And reversible heat generation, $\dot{Q}_{rev}$ is the entropic heat and can be either endothermic or exothermic at various state of charges (SOCs), with the signs being opposite for charge and discharge and is given by the equation

Equation 10: $$\boldsymbol{\dot{Q}_{rev} = T\Delta S\left(\frac{I}{nF}\right)}$$

Where I is the current in the cell, T is the temperature, ΔS is the total entropy change, n equals number of electrons per reaction, and F is the faraday constant. And total entropy change of cell is given by

$$\Delta S = \frac{nF\partial U}{\partial T}$$

Where, $\Delta S = \Delta S_c + \Delta S_a = nF\left(\frac{\partial U_c}{\partial T} + \frac{\partial U_a}{\partial T}\right)$

Where ΔS_c is entropy change corresponding to cathode and ΔS_a is the entropy change corresponding to anode; $\frac{\partial U}{\partial T}$ is the derivative of potential (U) with respect to the Temperature (T) and is called entropic heat coefficient or temperature coefficient. By adopting positive sign for exothermic heat, the sign of entropic heat during discharge is negative and during charge is positive for exothermic heat and opposite for endothermic heat. So, the $\dot{Q}_{rev}$ is also given by

Equation 11: $$\boldsymbol{\dot{Q}_{rev} = IT\left(\frac{\partial U}{\partial T}\right)}$$

By substituting $\dot{Q}_{rev}$ and $\dot{Q}_{irr}$ terms in Equation 7, we get

Equation 12: $$\boldsymbol{\dot{Q}_{gen} = I(V - U) + IT\left(\frac{\partial U}{\partial T}\right)}$$

Or,

$$\dot{Q}_{gen} = I^2R_{in} + IT\left(\frac{\partial U}{\partial T}\right)$$

Quantifying $\dot{Q}_{rev}$ needs to quantify entropic coefficient term $\left(\frac{\partial U}{\partial T}\right)$ and quantifying $\dot{Q}_{irr}$ needs to quantify R_{in}.

Quantifying reversible heat generation rate

From Equation 11, in order to quantify reversible heat generation we need to quantify the entropic coefficient which relates change in open circuit voltage (OCV) to change in temperature at various state of charges. CGR18650CG cylindrical Li-ion battery is charged and discharged at various C-rates: C/10, C/20, C/50, C/100 using the following protocol:

a) The cell is placed in the thermal chamber at 25^{o}C ambient temperature and rested for 5 hours for the cell to reach thermal equilibrium with ambient.
b) It is then charged at constant current rate with current corresponding to one of the above C-rate till it reaches the cut-off voltage of 4.2 V.
c) Then it is rested for 2 hours to reach both thermal and voltage equilibria.
d) It is then discharged at same current as charging till the lower cutoff voltage of 2.8 V is reached. This is repeated for 2 cycles at various ambient temperatures.

As we go for lower cycling rates, the voltage profile approaches OCV and the trends in the voltage reflects the trends in OCV. The shift in voltage profile decreases as we for lower C-rates and it is clear from Figure 31 that the shift in voltage profile is very less from C/20 to C/100 compared to the shift from C/10 to C/20 and it is very close to the open circuit voltage (OCV). So, the voltage profile during C/20 cycling rate is considered to represent the OCV and all the tests for OCV are carried at C/20 cycling rate. The 18650-cylindrical battery is charged and discharged using following protocol:

a) The cell is placed in the thermal chamber at desired ambient temperature (25^{o}C, 40^{o}C and 50^{o}C) and rested for 5 hours for the cell to reach thermal equilibrium with ambient.

b) It is then charged at constant current rate with current corresponding to C/20 rate till it reaches the cut-off voltage of 4.2V.

c) Then it is rested for 2 hours to reach both thermal and voltage equilibria.

d) It is then discharged at same current as charging till the lower cutoff voltage of 2.8V is reached. This is repeated for 2 cycles at various ambient temperatures.

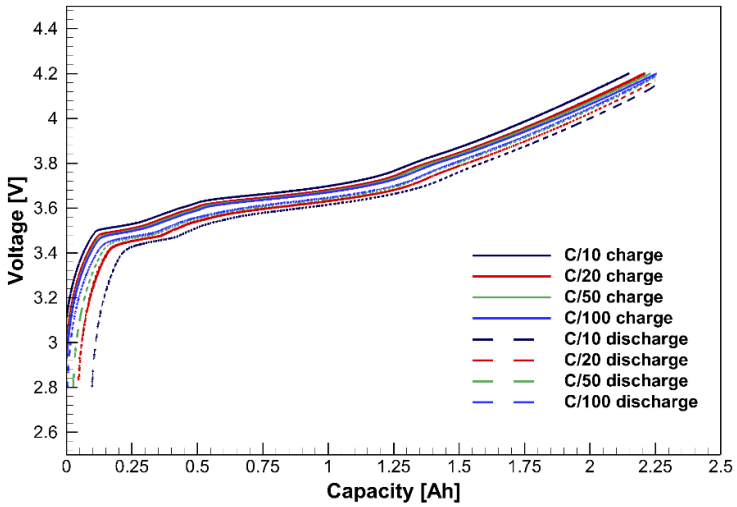

Figure 31. Voltage profiles during charging and discharging the cell at C/20-rate with different ambient temperatures.

Figure 32 shows the voltage vs. capacity profiles for charging and discharging the cell at C/20 rate at various ambient temperatures: 25^{o}C, 40^{o}C, 50^{o}C. It can be seen from Figure 32 that the variation of voltage is very small over a wide range of temperatures i.e. less than 5 mV over 25^{o}C to 50^{o}C while operating at very low C-rate (C/20-rate). Since the change in voltage is very less over wide range of temperatures and as we are assuming this voltage very close to

open circuit voltage, we can say entropic coefficient $\left(\frac{dU}{dT}\right)$ value is very low at C/20 rate. The contribution of reversible entropic heat is major at low C-rates like C/20 rate and irreversible ohmic heat is negligible. But based on variation in OCV value with temperature at C/20 rate, the reversible heat generation rate appears to be very small, so if we go for higher C-rates (operating rates generally used in all applications) where contribution of reversible heat is very low and irreversible heat is a major contributor, we can safely neglect the contribution of reversible heat at higher operational rates. So, we need to quantify only irreversible heat generation rate and can assume it to be total heat generation rate if we are operating the battery at higher C-rates.

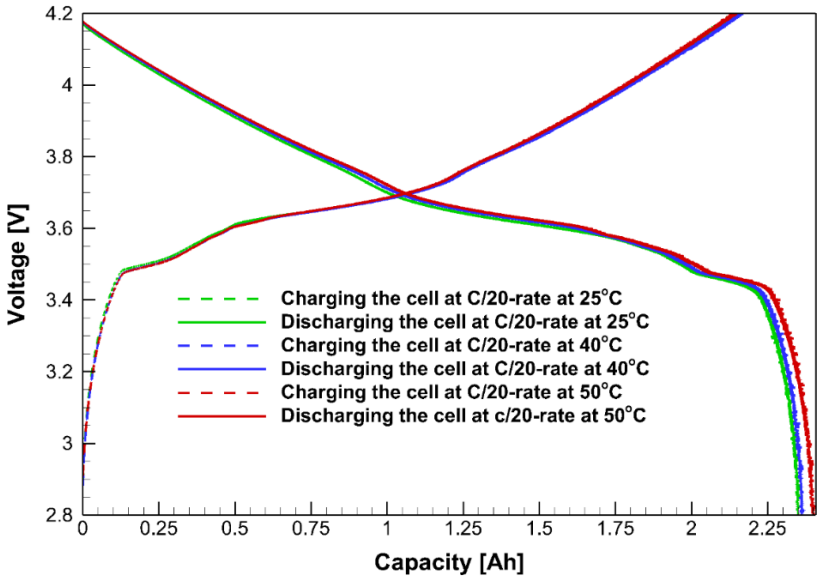

Figure 32. Voltage vs. capacity profiles for discharging the cell at C/20 rate at various ambient temperatures: 25ºC, 40ºC, 50ºC.

Quantifying irreversible heat generation rate

Total heat generation values at various C-rates are found to have a direct relation with square of current at that C-rate.

Equation 13: $$\dot{Q}_{gen} \propto I^2$$

$$\dot{Q}_{gen} = pI^2$$

p is a proportionality constant and the values of p for heat generation rates at various cycling rates are found to be close to each other. The similarity between Equation 8 and Equation 13 shows that internal resistance value might be the proportionality constant, so internal resistance values at various operation rates are calculated to investigate their relation with heat generation rates. The current pulse is applied while charging/discharging to calculate the internal resistance.

Current pulse protocol

a) During the charging-current pulse, a positive current of 3.375 A is provided for 100 ms and then immediately rested for 400 ms.
b) During the discharging-current pulse, a negative current of 3.375 A is provided for 100 ms and then immediately rested for 400 ms

Protocol used for measuring the internal resistance

The following protocol is used to cycle the cell using the arbin cycler to calculate internal resistances at various state of charges during charging and discharging.

a) The cell is setup with arbin system and is provided with initial rest of 2 hours to allow the cell to reach thermal equilibrium with room temperature ambient.

b) At the beginning of charging a charging current pulse is provided which is later used to calculate internal resistance and then charging is continued at desired C-rate till charge capacity is reached to 50 percent and then another charging current pulse is provided. Then the charging is continued till the voltage reaches upper cut-off voltage of 4.2 V. At the end of charge, a charging current pulse is applied again.

c) The cell is rested for 2 hours to allow it to reach thermal and voltage equilibria.

d) Just before discharge a discharge current pulse is provided and the cell is continued to discharge at the same rate as of charging. After the discharge capacity reaches the 50 percent of total discharge capacity, another discharge pulse is applied and then the cell is continued to discharge till the voltage reaches lower cut-off voltage of 2.8 V. At the end of discharge, another discharge current pulse is applied and then the cell is rested for 2 hours.

e) This process is repeated for 3 cycles for each C-rate: C/5, 1C, 2C, 3C and 4C.

The current pulses are applied as shown in Figure 33 and then the internal resistance can be calculated from the current pulse as shown in Figure 34. By rearranging Equation 9

Equation 14: $$\boldsymbol{R_{int} = \frac{V_1 - V_2}{I_1 - I_2} = \frac{\Delta V}{\Delta I}}$$

Where V_1 is the terminal voltage of the cell at end of the application of current during the pulse period, V_2 is the voltage at the start of rest period during pulse, I_1 is the current value at the end of application of current and I_2 is the current at the start of rest period during pulse period.

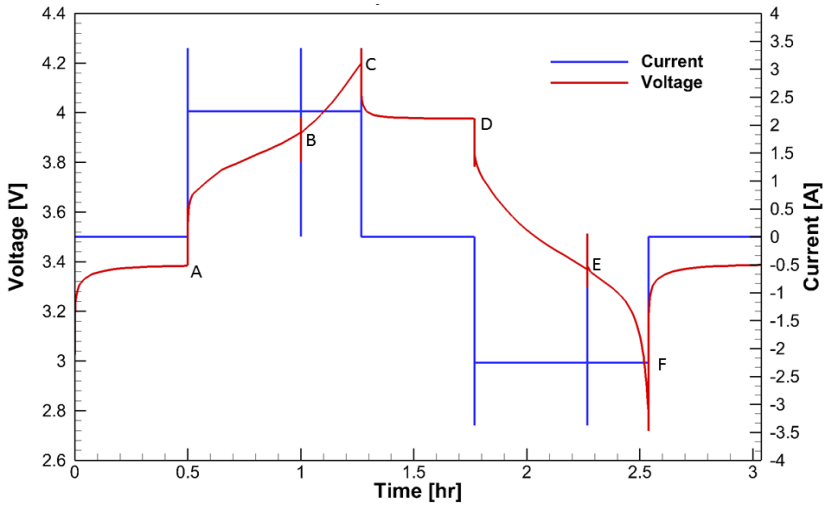

Figure 33. Voltage, current vs. time plot for "charge-rest-discharge-rest" loop at 1C-rate. A, B, C, D, E, F are the points where current pulses are applied.

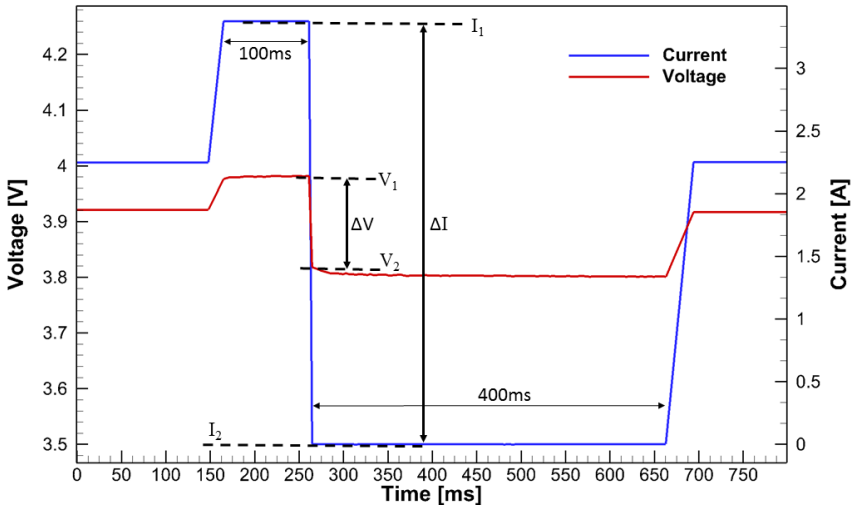

Figure 34. Voltage, current vs. time for current pulse at point B during charging as shown in Figure 33.

Results and discussions

The average values of internal resistance calculated at various SOCs for different C-rates: C/5, C/2, 1C, 2C are as shown in Table 6.

Table 6. Average internal resistance values at various SOC during cycling of the battery at different C-rates.

Various SOCs	Average value of internal resistance (r) ($m\Omega$)			
	C/5 - rate	C/2 – rate	1C - rate	2C - rate
A) Before charging	52.61	53.49	52.33	51.57
B) During charging (at 50% charge capacity)	49.77	50.26	48.49	46.30
C) After charging	48.05	49.42	47.26	45.71
D) Before discharging	48.32	50.22	49.99	50.06
E) During discharging (at 50% discharge capacity)	50.04	52.31	51.44	51.48
F) After discharging	52.92	55.18	53.43	52.01

Table 7. Internal resistances calculated from total heat generation rates and by applying current pulse for different C-rates.

C-rate	Internal resistance $\left(\frac{\dot{Q}_{gen}}{I^2}\right)$	Average internal resistance $\left(\frac{\Delta V}{\Delta I}\right)$
C/2	52.938	53.39
1C	52.345	52.66
2C	49.666	49.27

The internal resistance values calculated from total heat generation rate and by applying current pulse for various C-rates are as shown in Table 7. The internal resistance values at

various state of charges over 3-cycles during charging and discharging the cells at various C-rates: C/2 to 4C.

Table 8. Internal resistance values at various SOC during charge-discharge cycles at C/2-rate.

Cycle no.	Internal resistance ($m\Omega$)							
	Before charge	**At 50% of charge**	**After charge**	**Before discharge**	**At 50% of discharge**	**After discharge**	**Average value**	**Standard deviation**
Cycle 1	63.53	53.36	50.83	43.13	44.33	63.95	53.19	8.24
Cycle 2	63.31	54.20	51.25	42.94	44.51	63.96	53.37	8.19
Cycle 3	63.52	54.20	51.04	43.63	44.74	63.74	53.48	8.02

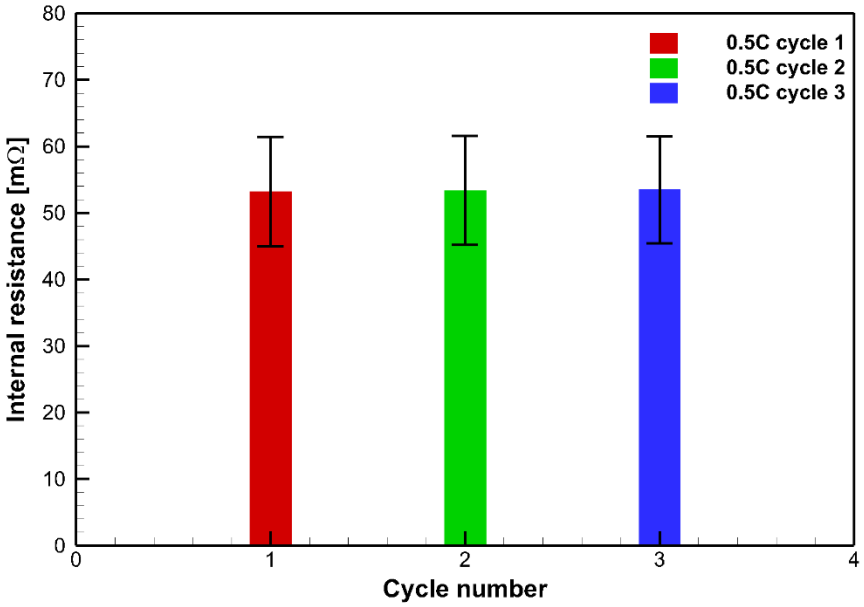

Figure 35. Average internal resistance for each cycle over 3 charge-discharge cycles at C/2 rate.

Table 9. Internal resistance values at various SOC during charge-discharge cycles at 1C-rate.

Cycle no.	Internal resistance ($m\Omega$)							
	Before charge	**At 50% of charge**	**After charge**	**Before discharge**	**At 50% of discharge**	**After discharge**	**Average value**	**Standard deviation**
Cycle 1	60.35	51.46	49.55	43.36	44.58	63.32	52.11	7.45
Cycle 2	60.55	52.30	49.55	43.19	44.74	63.73	52.35	7.59
Cycle 3	60.98	52.71	49.96	43.59	44.77	63.94	52.66	7.61

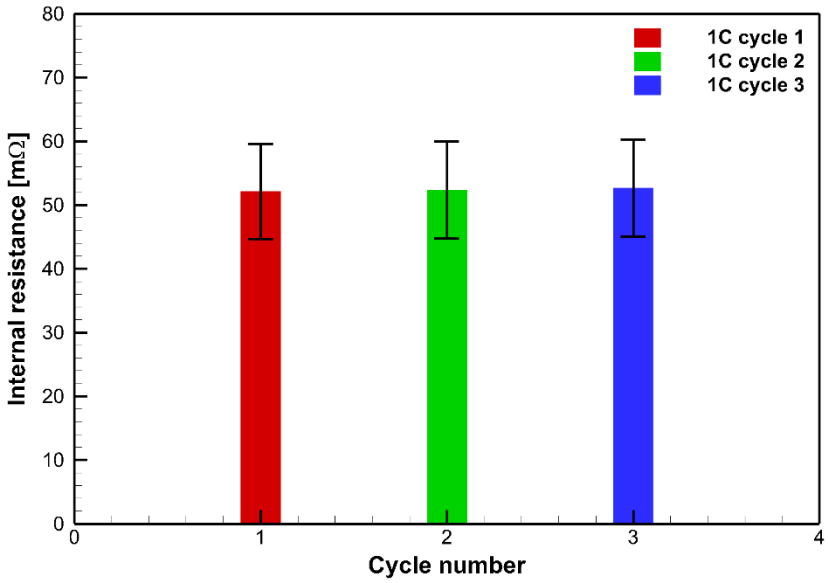

Figure 36. Average internal resistance for each cycle over 3 charge-discharge cycles at 1C rate.

Table 10. Internal resistance values at various SOC during charge-discharge cycles at 2C-rate.

Cycle no.	Internal resistance ($m\Omega$)							
	Before charge	At 50% of charge	After charge	Before discharge	At 50% of discharge	After discharge	Average value	Standard deviation
Cycle 1	52.94	48.70	46.79	42.71	45.19	59.50	49.31	5.53
Cycle 2	52.51	48.27	46.59	43.64	45.21	59.08	49.22	5.21
Cycle 3	52.70	48.47	46.63	43.13	45.27	59.28	49.24	5.53

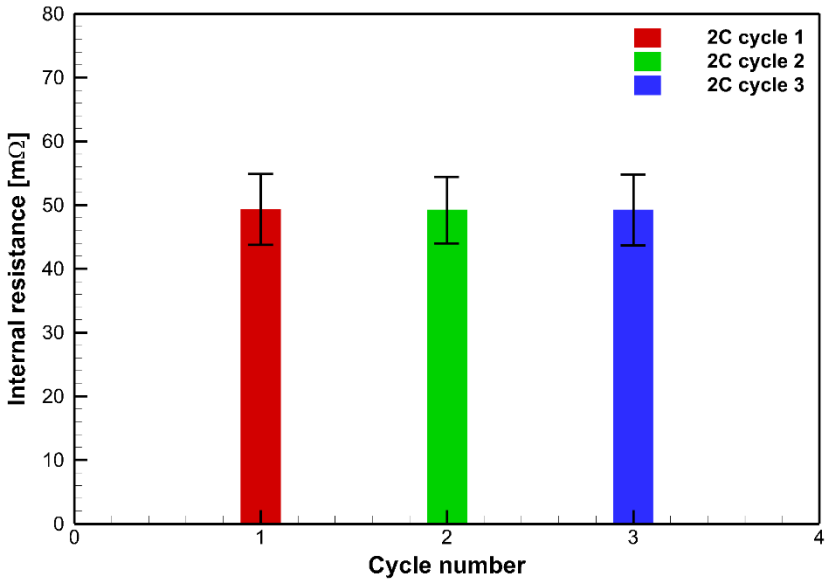

Figure 37. Average internal resistance for each cycle over 3 charge-discharge cycles at 2C rate.

Table 11. Internal resistance values at various SOC during charge-discharge cycles at 3C-rate.

Cycle no.	Internal resistance ($m\Omega$)							
	Before charge	**At 50% of charge**	**After charge**	**Before discharge**	**At 50% of discharge**	**After discharge**	**Average value**	**Standard deviation**
Cycle 1	50.60	48.27	46.80	43.16	44.60	57.59	48.50	4.72
Cycle 2	51.03	47.86	47.01	43.86	45.24	58.66	48.94	4.88
Cycle 3	51.24	48.27	46.80	43.63	45.48	59.29	49.12	5.12

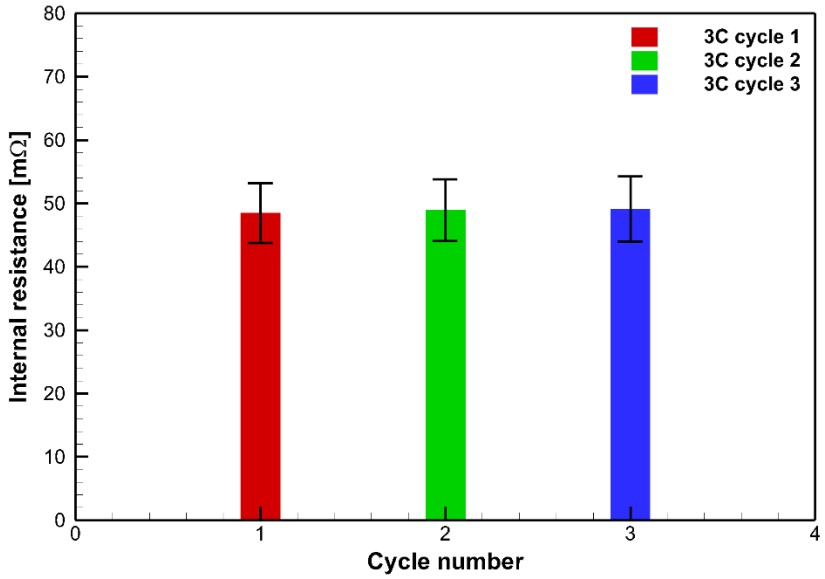

Figure 38. Average internal resistance for each cycle over 3 charge-discharge cycles at 3C rate.

Table 12. Internal resistance values at various SOC during charge-discharge cycles at 4C-rate.

Cycle no.	Internal resistance ($m\Omega$)							
	Before charge	At 50% of charge	After charge	Before discharge	At 50% of discharge	After discharge	Average value	Standard deviation
Cycle 1	53.14	52.30	51.88	43.65	47.90	60.76	51.61	5.22
Cycle 2	55.47	54.41	53.78	45.23	47.00	63.32	53.21	5.93
Cycle 3	55.68	54.84	54.62	44.97	46.33	63.75	53.37	6.28

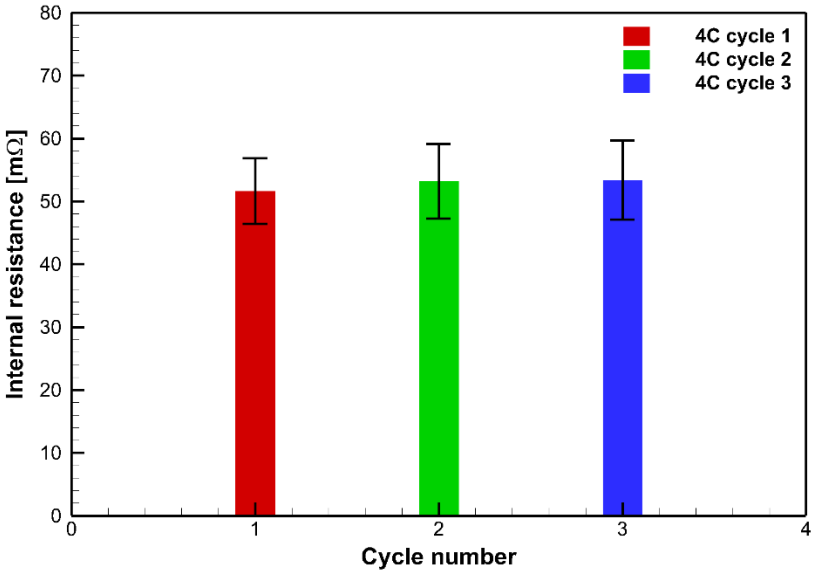

Figure 39. Average internal resistance for each cycle over 3 charge-discharge cycles at 4C rate.

Table 13. Average values of internal resistances over 3 charge – discharge cycles at various C-rates.

C-rate	Average value of internal resistance ($m\Omega$)	Standard deviation
C/2	53.39	0.13
1C	52.66	0.22
2C	49.27	0.04
3C	48.96	0.26
4C	52.73	0.79

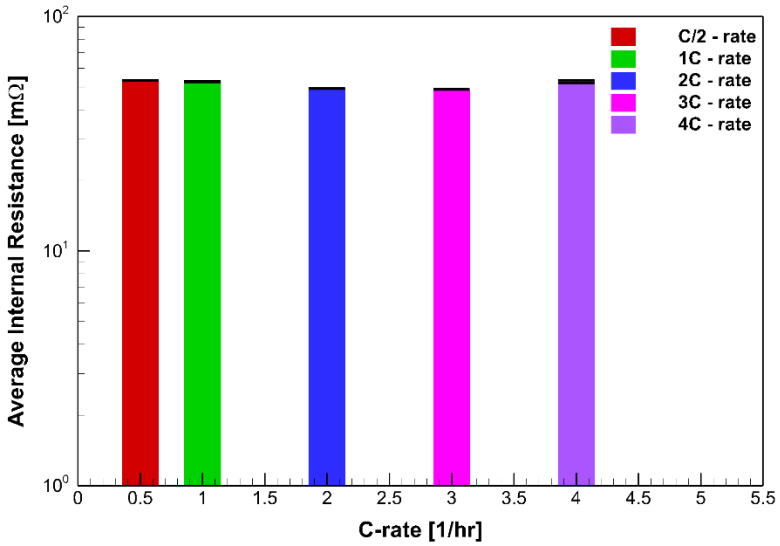

Figure 40. Average internal resistance of all 3 charge-discharge cycles for C/2, 1C, 2C, 3C and 4C rates.

From Figure 35 to Figure 40 and Table 6 to Table 13 data, it can be concluded that the internal resistance values are close to each other also close to the internal resistance values calculated from total heat generation rates while the cell is operating at various C-rates: C/2 to 4C and finding internal resistance at any one of the C-rate is sufficient as it reflects internal

resistance values at other C-rates. So, by calculating the average internal resistance value at any one of the C-rate, we can quantify the total heat generation rate during an electrochemical operation the cell at various C-rates. Now we know the C-rate dependence of internal resistance, the effect of capacity fade needs to be determined.

Effect of capacity fade

To investigate the effect of capacity fade, cells are faded and internal resistance values are measured using following procedure:

1. The fresh 18650 cells are taken and are cycled at three different C-rates C/2, 1C and 2C till three different capacity fades of 5%, 10% and 15% are reached at each C-rate. Each cell is faded to one selected percentage of capacity fade while cycling at one selected C-rate.
2. After respective capacity fades, internal resistance values are calculated by applying current pulse while charging and discharging cells at 1C-rate and from the total heat generation rate calculated by inverse heat transfer analysis.

Internal resistance values after capacity fade

The internal resistances calculated for the cell cycled to different percentage capacity fades at various cycling rates are shown from Table 14 to Table 22 and Figure 41 to Figure 49. Table 23 shows the total heat generation rate values and internal resistances calculated from the total heat generation rates and by applying current pulse for the cells cycled to various percentage capacity fades at various C-rates. Both total heat generation rates and internal resistance values by applying current pulse are calculated while cell is cycled with 'charge-rest-discharge-rest' loop at 1C-rate. Also it is clear that the amount of total heat generation rate slightly increased with increase in the amount of capacity fade occurring in the cell at different

cycling rates. And the internal resistance values calculated by applying the current pulse are closely related to the total heat generation rates. Figure 50 to Figure 52 shows the average internal resistance values over 2 cycles after capacity fade of 5%, 10% and 15% at C/2, 1C and 2C rates respectively.

Table 14. Internal resistance values during 'charge-discharge' cycle after 5% capacity fade at C/2-rate.

Cycle no.	Internal resistance ($m\Omega$)							
	Before charge	**At 50% of charge**	**After charge**	**Before discharge**	**At 50% of discharge**	**After discharge**	**Average value**	**Standard deviation**
Cycle 1	53.46	50.15	48.75	51.20	52.33	55.55	51.91	2.21
Cycle 2	53.99	50.61	49.17	51.40	52.99	55.78	52.32	2.20

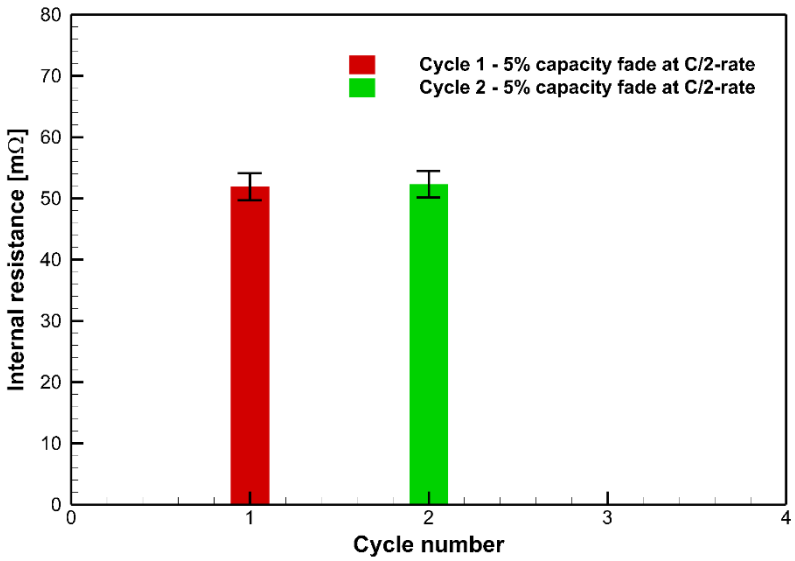

Figure 41. Average internal resistance values for each cycle over 2 Charge-discharge cycles after capacity fade of 5% at C/2 rate.

Table 15. Internal resistance values during 'charge-discharge' cycle after 10% capacity fade at C/2-rate.

Cycle no.	Internal resistance ($m\Omega$)							
	Before charge	At 50% of charge	After charge	Before discharge	At 50% of discharge	After discharge	Average value	Standard deviation
Cycle 1	53.32	50.79	49.60	52.19	53.22	55.35	52.41	1.85
Cycle 2	54.36	51.44	49.45	52.45	53.12	55.64	52.74	1.99

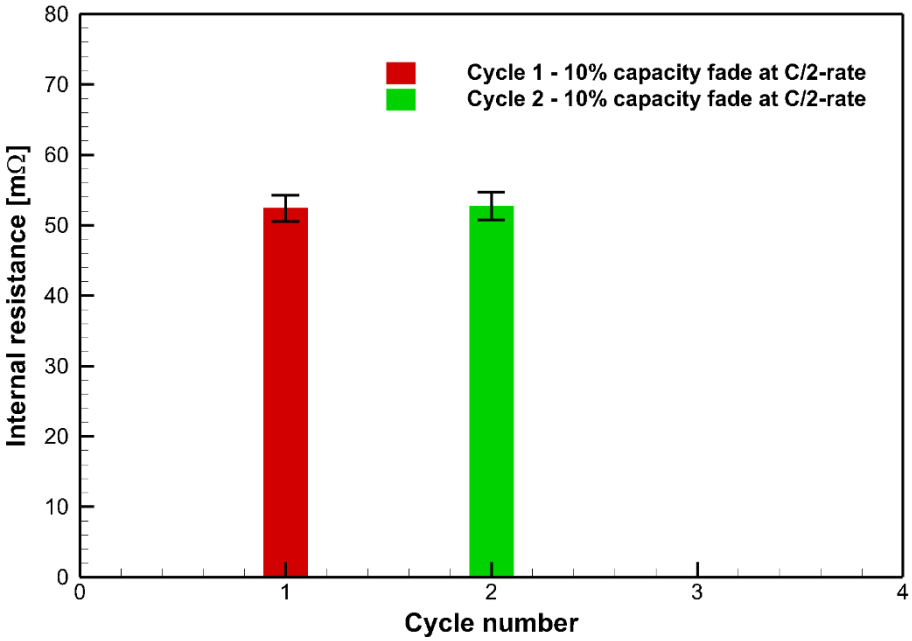

Figure 42. Average internal resistance for each cycle over 2 charge-discharge cycles after capacity fade of 10% at C/2 rate.

Table 16. Internal resistance values during 'charge-discharge' cycle after 15% capacity fade at C/2-rate.

Cycle no.	Internal resistance ($m\Omega$)							
	Before charge	At 50% of charge	After charge	Before discharge	At 50% of discharge	After discharge	Average value	Standard deviation
Cycle 1	59.21	56.37	54.67	58.37	59.08	61.73	58.24	2.24
Cycle 2	60.50	57.04	55.23	58.23	59.35	61.63	58.68	2.12

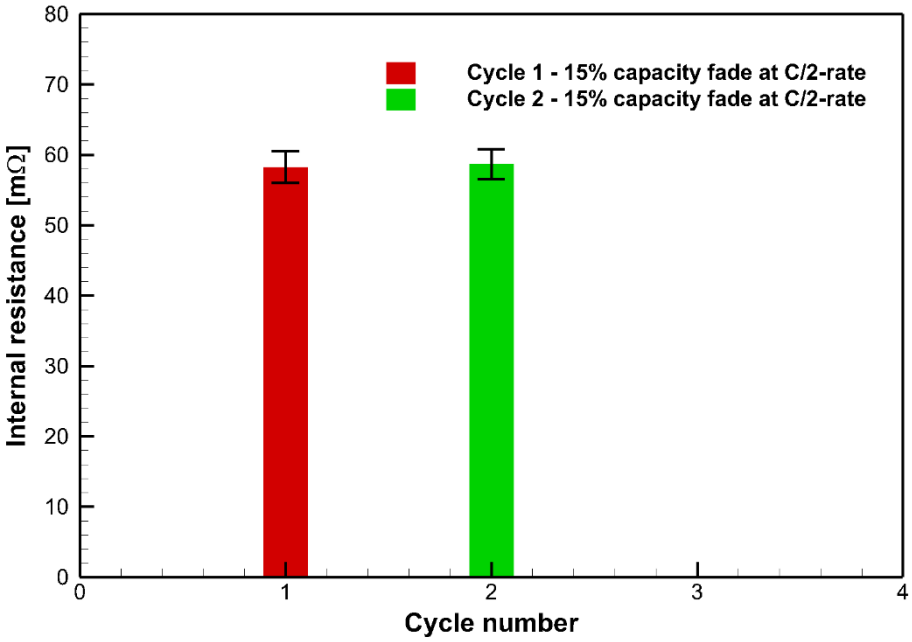

Figure 43. Average internal resistance for each cycle over 2 charge-discharge cycles after capacity fade of 15% at C/2 rate.

Table 17. Internal resistance values during 'charge-discharge' cycle after 5% capacity fade at 1C-rate.

Cycle no.	Internal resistance ($m\Omega$)							
	Before charge	**At 50% of charge**	**After charge**	**Before discharge**	**At 50% of discharge**	**After discharge**	**Average value**	**Standard deviation**
Cycle 1	61.16	57.81	56.24	59.01	60.14	62.68	59.50	2.12
Cycle 2	61.88	58.19	56.50	58.99	60.05	62.55	59.69	2.08

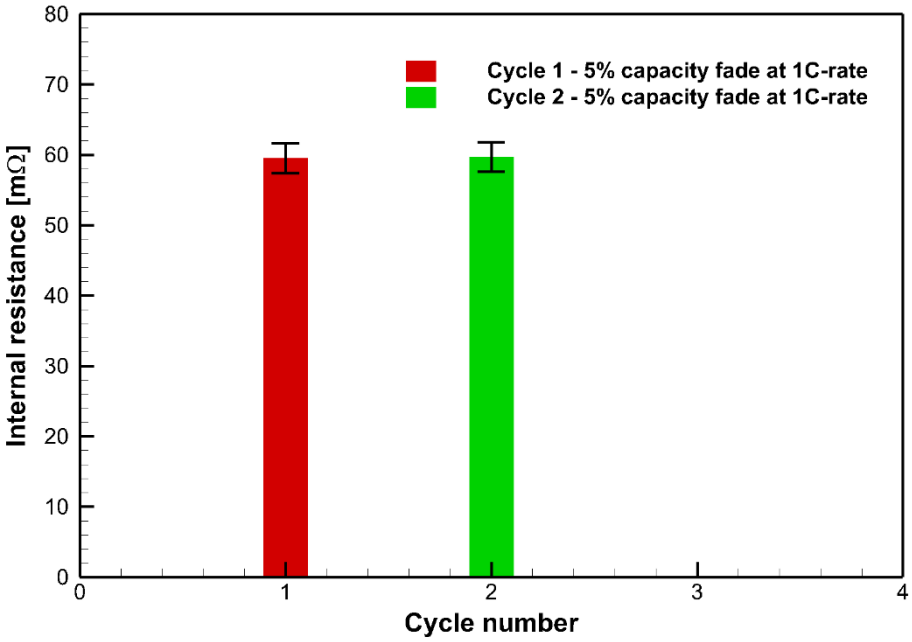

Figure 44. Average internal resistance for each cycle over 2 charge-discharge cycles after capacity fade of 5% at 1C rate.

Table 18. Internal resistance values during 'charge-discharge' cycle after 10% capacity fade at 1C-rate.

Cycle no.	Internal resistance ($m\Omega$)							
	Before charge	At 50% of charge	After charge	Before discharge	At 50% of discharge	After discharge	Average value	Standard deviation
Cycle 1	53.84	50.98	48.77	52.43	53.42	56.15	52.60	2.31
Cycle 2	54.80	51.09	49.07	52.53	53.32	56.63	52.91	2.44

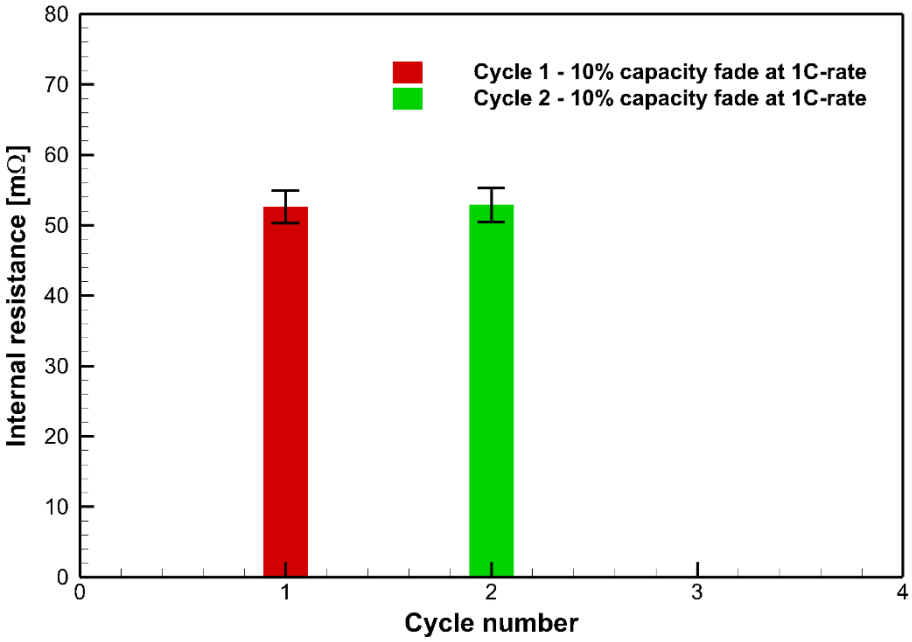

Figure 45. Average internal resistance for each cycle over 2 charge-discharge cycles after capacity fade of 10% at 1C rate.

Table 19. Internal resistance values during 'charge-discharge' cycle after 15% capacity fade at 1C-rate.

Cycle no.	Internal resistance ($m\Omega$)							
	Before charge	At 50% of charge	After charge	Before discharge	At 50% of discharge	After discharge	Average value	Standard deviation
Cycle 1	56.91	53.78	52.13	55.71	56.55	58.49	55.59	2.09
Cycle 2	58.25	53.97	52.15	55.76	56.78	58.86	55.96	2.34

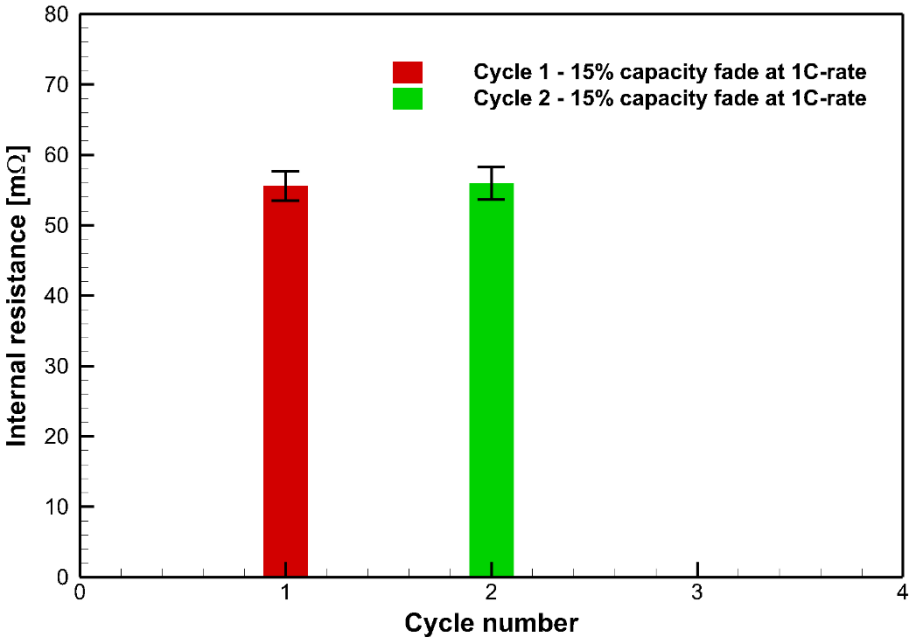

Figure 46. Average internal resistance for each cycle over 2 charge-discharge cycles after capacity fade of 15% at 1C rate.

Table 20. Internal resistance values during 'charge-discharge' cycle after 5% capacity fade at 2C-rate.

Cycle no.	Internal resistance ($m\Omega$)							
	Before charge	At 50% of charge	After charge	Before discharge	At 50% of discharge	After discharge	Average value	Standard deviation
Cycle 1	53.25	49.95	47.99	51.25	52.47	54.82	51.62	2.22
Cycle 2	54.13	50.05	48.18	51.58	52.56	55.10	51.93	2.34

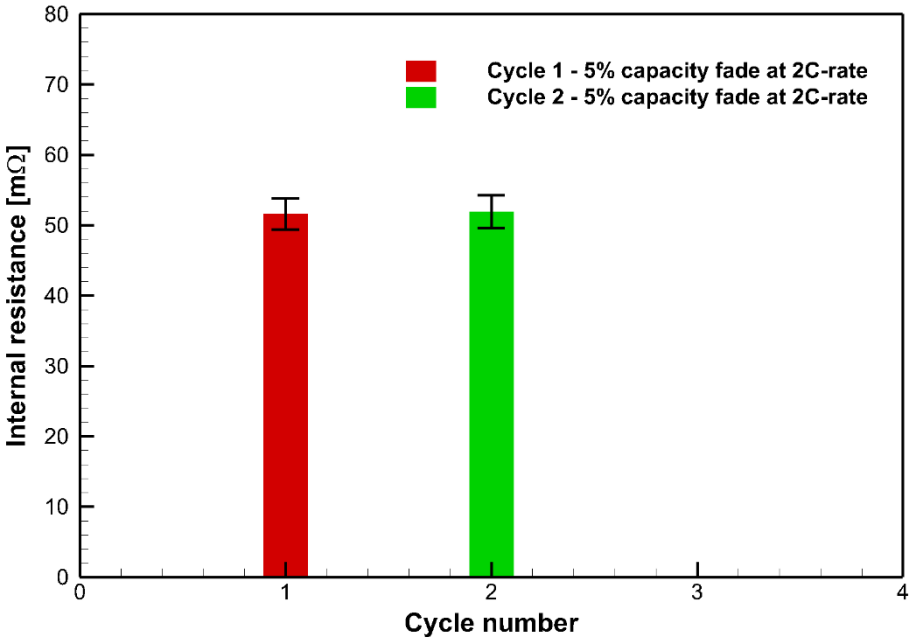

Figure 47. Average internal resistance for each cycle over 2 charge-discharge cycles after capacity fade of 5% at 2C rate.

Table 21. Internal resistance values during 'charge-discharge' cycle after 10% capacity fade at 2C-rate.

Cycle no.	Internal resistance ($m\Omega$)							
	Before charge	**At 50% of charge**	**After charge**	**Before discharge**	**At 50% of discharge**	**After discharge**	**Average value**	**Standard deviation**
Cycle 1	56.65	53.54	52.17	55.24	56.33	58.83	55.46	2.16
Cycle 2	57.77	54.32	52.06	55.20	56.12	58.53	55.67	2.15

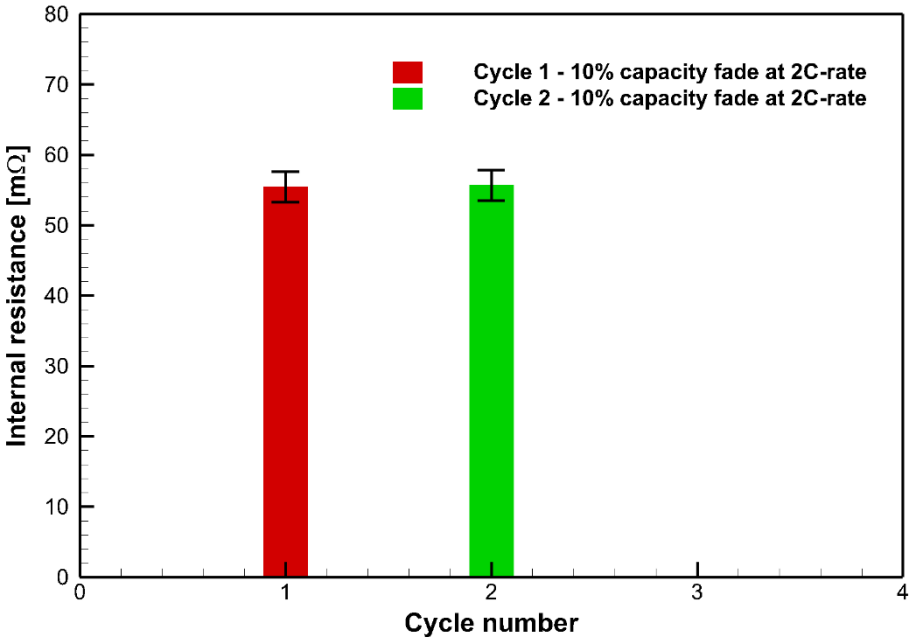

Figure 48. Average internal resistance for each cycle over 2 charge-discharge cycles after capacity fade of 10% at 2C rate.

Table 22. Internal resistance values during 'charge-discharge' cycle after 15% capacity fade at 2C-rate.

Cycle no.	Internal resistance ($m\Omega$)							
	Before charge	At 50% of charge	After charge	Before discharge	At 50% of discharge	After discharge	Average value	Standard deviation
Cycle 1	55.59	52.33	50.66	53.93	55.13	57.71	54.22	2.25
Cycle 2	56.57	52.80	51.22	54.35	55.46	57.72	54.68	2.19

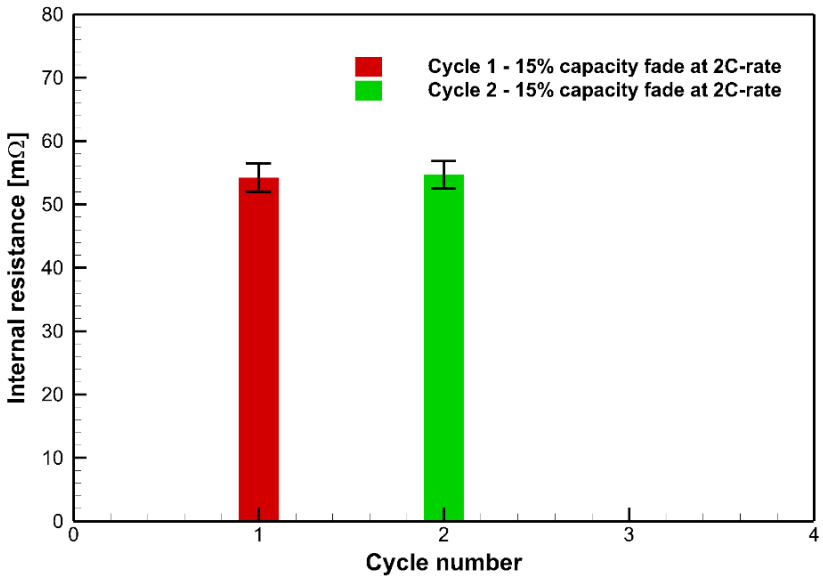

Figure 49. Average internal resistance for each cycle over 2 charge-discharge cycles after capacity fade of 15% at 2C rate.

Table 23. Average internal resistance values calculated from total heat generation rate and by applying current pulse.

Cycling rate	Capacity fade in % of theoretical capacity	Average internal resistance by applying current pulse ($m\Omega$)
C/2	5	51.19
	10	52.74
	15	58.24
1C	5	59.60
	10	52.60
	15	55.59
2C	5	60.29
	10	52.91
	15	54.74

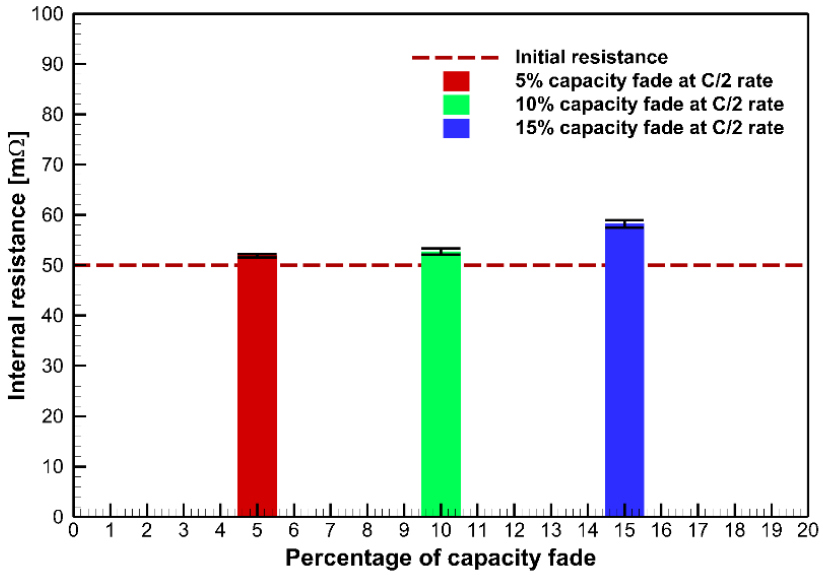

Figure 50. Average internal resistance of 2 charge-discharge cycles after capacity fade of 5%, 10% and 15% at C/2 cycling rate.

From Figure 50 to Figure 53, It can be seen that the internal resistance value increases continuously from fresh cell to cell faded to 15% while cycling the cell at lower C-rates which is due to irreversible consumption of Lithium in the formation of solid electrolyte interphase (SEI) layer which necessarily increases resistance to the flow of Lithium ions.

While cycling at higher C-rates internal resistance increases during early stages of capacity fade due to the irreversible consumption of Lithium in the formation of SEI layer, but later decreases which might be due to the crack formation of SEI layer taking place which is predominant at higher C-rates causing more decrease in internal resistance as we go for higher C-rate cycling.

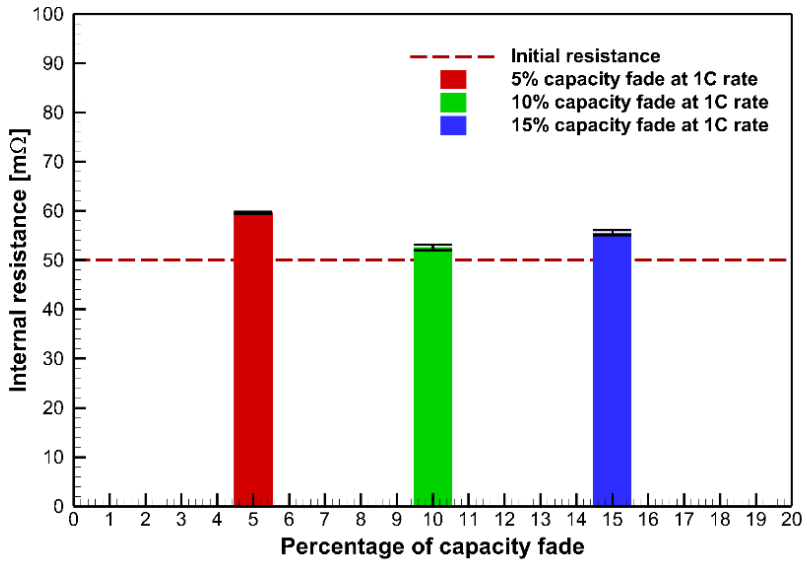

Figure 51. Average internal resistance of 2 charge-discharge cycles after capacity fade of 5%, 10% and 15% at 1C cycling rate.

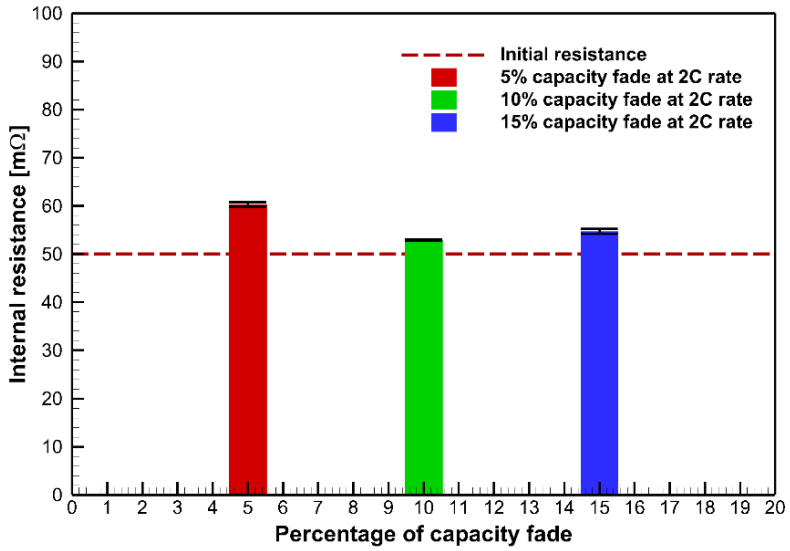

Figure 52. Average internal resistance of 2 charge-discharge cycles after capacity fade of 5%, 10% and 15% at 2C cycling rate.

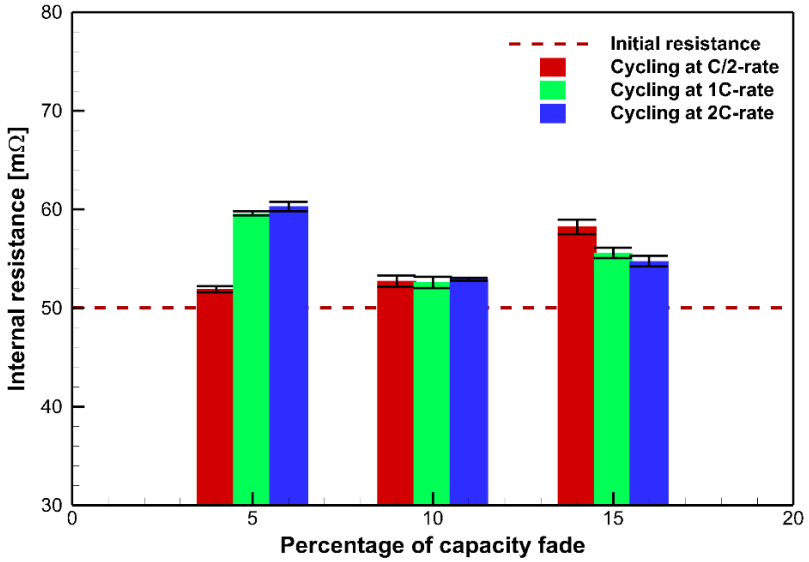

Figure 53. Average internal resistance after various amounts of capacity fade when cycled at various C-rates.

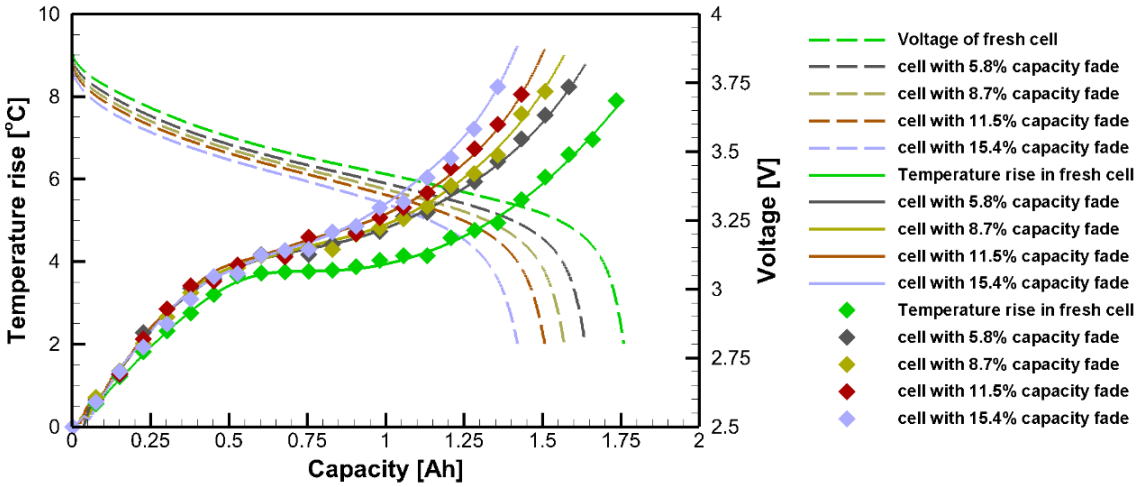

Figure 54. Temperature rise and voltage profiles in the cell during discharge after various amounts of capacity fade occurring at 1C-rate.

Figure 54 shows the temperature and voltage profile of the cell during discharge after various amounts of capacity fades. The maximum temperature at the end of the discharge increases with capacity fade and this rate of increase is more during initial fading, up to 5% fade, and is slightly less in later stages of fading, from 5% to 10%. Since the maximum temperature in the cell corresponds to the total heat generation in the cell the trends observed in temperature profiles can be related to the heat generation. Since the heat generation rate is directly related to internal resistance, it can be inferred that the rate of increase in internal resistance is high during initial capacity fading but decreases during the later stages of fading in the cell.

CHAPTER V

CONCLUSIONS AND FUTURE SCOPE

The total heat generation rates in an 18650 cylindrical Li-ion cell during an electrochemical operation has been successfully quantified with proposed experimental setup based on inverse heat transfer analysis without using a calorimeter.

The convective heat transfer coefficient is obtained by correlating the temperature data during rest period with time using energy balance equation which is later used for quantifying heat generation rates. The goodness of correlation given by R-square values shows to have a good data correlation. The surface temperature of the cell increases with SOC as charging/discharging of the cell proceeds and it is more prominent at higher C-rates. The increase in surface temperature of the cell is more at the beginning of the discharge then decreases towards the middle of the discharge and again increases at the end of the discharge. During charging, the increase in surface temperature is more at the beginning of charge and decreases towards the end of charge. The maximum surface temperature reached by the cell increases as we increase the C-rate of charging/discharging of the cell. The maximum temperature reached by the cell at C/2 discharging rate is around 0.7^oC while it is around 25^oC during 3C discharging rate. From voltage profiles, it can be seen the capacity of the cell decreases as the C-rate of charging/discharging operation increases.

The total heat generation rate is quantified by correlating the surface temperature data of the cell during charging and discharging with energy balance equation. The total heat generation rate increases with C-rate during both charging and discharging. The increase is from 0.0179 W at C/2-rate to 1.6188 W at 3C-rate during charging and 0.0125 W at C/2-rate to 1.7354 W at 3C-rate during discharging. The heat generation rate is high at the beginning

of the charge and increases slightly to the middle of charge and decreases to the end of charge. This is due to the high charge transfer resistance at the beginning of the charge which decreases in later stages of the charge process. During discharge the heat generation rate is high at the beginning, decreases to the middle of the discharge and again increases to the end of discharge. This is due to the high charge transfer resistance at the beginning of discharge, which later decreases and large over-potentials due to polarization and ohmic resistances developed at the end of the discharge.

Contribution of reversible entropic heat term towards the total heat generation rate is found to be negligible during the operation of the cell at higher C-rates. Irreversible ohmic heat is found to be major contributor towards total heat generation rate at higher cycling rates and it is closely related to the internal resistance of the cell. The internal resistance of the cell is found to be independent of C-rate, used during charging and discharging, with standard deviation of 1.88 $m\Omega$ for average internal resistances calculated over charge-discharge cycle for various C-rates. With capacity fade occurring at low C-rate cycling, the internal resistance increases with capacity fade due to the irreversible consumption of lithium in the formation of SEI layer. While cycling at higher C-rates the internal resistance increased initially with capacity fade due to irreversible consumption of lithium in the formation of SEI layer, but later internal resistance decreased till certain amount of fade due to the crack formation in SEI layer taking place and this is more predominant with increase in C-rate. The rate of increase in maximum temperature of the cell during discharge is more during initial stages of capacity fade and this rate decreases in later stages of capacity fade which can be related to high rate of increase in internal resistance during initial capacity fading and decrease in this rate during later stages of capacity fading.

Investigating the effect of ambient temperature on the amount of heat generation rates in a cell cycling at various charging and discharging rates could provide more insight to implement the Battery Thermal Management System (BTMS) under varying environmental conditions. Also, considering the effect of ambient temperature on capacity fade of a cell when fading at different cycling rates and its effect on the internal resistance of the cell associated with such fade as well could be an interesting extension to the present study.

REFERENCES

[1] R. Marom, S. F. Amalraj, N. Leifer, D. Jacob, and D. Aurbach, "A review of advanced and practical lithium battery materials," *Journal of Materials Chemistry*, 10.1039/C0JM04225K vol. 21, no. 27, pp. 9938-9954, 2011.

[2] J.-M. Tarascon and M. Armand, "Issues and challenges facing rechargeable lithium batteries," *Nature*, vol. 414, no. 6861, pp. 359-367, 2001.

[3] C. D. Rahn and C.-Y. Wang, *Battery systems engineering*. John Wiley & Sons, 2013.

[4] W. van Schalkwijk and B. Scrosati, *Advances in lithium-ion batteries*. Springer Science & Business Media, 2007.

[5] "Lithium ion battery overview," *Lighting Global*, no. 10, Accessed on: 02-07-2017Available: https://www.lightingglobal.org/wp-content/uploads/2012/05/67_Issue10_Lithium-ionBattery_TechNote_final.pdf

[6] V. Etacheri, R. Marom, R. Elazari, G. Salitra, and D. Aurbach, "Challenges in the development of advanced Li-ion batteries: a review," *Energy & Environmental Science*, vol. 4, no. 9, pp. 3243-3262, 2011.

[7] (February 7). *Battery University*. Available: http://batteryuniversity.com/learn/article/types_of_lithium_ion

[8] (February 7). *Battery University*. Available: http://batteryuniversity.com/learn/article/types_of_battery_cells

[9] C. R. Birkl, M. R. Roberts, E. McTurk, P. G. Bruce, and D. A. Howey, "Degradation diagnostics for lithium ion cells," *Journal of Power Sources*, vol. 341, pp. 373-386, 2/15/ 2017.

[10] Z. Kleinman, "Why do lithium batteries explode?," in *BBC*, ed, 2016.

[11] X. Zhang, "Thermal analysis of a cylindrical lithium-ion battery," *Electrochimica Acta*, Article vol. 56, pp. 1246-1255, 1/1/2011 2011.

[12] S. Chen, C. Wan, and Y. Wang, "Thermal analysis of lithium-ion batteries," *Journal of Power Sources,* vol. 140, no. 1, pp. 111-124, 2005.

[13] L. O. Valøen and J. N. Reimers, "Transport properties of LiPF6-based Li-ion battery electrolytes," *Journal of The Electrochemical Society,* vol. 152, no. 5, pp. A882-A891, 2005.

[14] J. Newman and K. E. Thomas-Alyea, *Electrochemical systems*. John Wiley & Sons, 2012.

[15] M. Doyle, T. F. Fuller, and J. Newman, "Modeling of galvanostatic charge and discharge of the lithium/polymer/insertion cell," *Journal of the Electrochemical Society,* vol. 140, no. 6, pp. 1526-1533, 1993.

[16] P. Georén and G. Lindbergh, "Characterisation and modelling of the transport properties in lithium battery polymer electrolytes," *Electrochimica Acta,* vol. 47, no. 4, pp. 577-587, 11/1/ 2001.

[17] C. Wang, W. Gu, and B. Liaw, "Micro-Macroscopic Coupled Modeling of Batteries and Fuel Cells I. Model Development," *Journal of the Electrochemical Society,* vol. 145, no. 10, pp. 3407-3417, 1998.

[18] V. R. Subramanian, V. D. Diwakar, and D. Tapriyal, "Efficient macro-micro scale coupled modeling of batteries," *Journal of The Electrochemical Society,* vol. 152, no. 10, pp. A2002-A2008, 2005.

[19] S.-C. Chen, Y.-Y. Wang, and C.-C. Wan, "Thermal analysis of spirally wound lithium batteries," *Journal of the Electrochemical Society,* vol. 153, no. 4, pp. A637-A648, 2006.

[20] D. Bernardi, E. Pawlikowski, and J. Newman, "A general energy balance for battery systems," *Journal of the electrochemical society,* vol. 132, no. 1, pp. 5-12, 1985.

[21] Y. Chen and J. W. Evans, "Thermal analysis of Lithium-Ion batteries," *Journal of the Electrochemical Society,* vol. 143, no. 9, pp. 2708-2712, 1996.

[22] U. von Sacken, E. Nodwell, A. Sundler, and J. Dahn, "Comparative thermal stability of carbon intercalation anodes and lithium metal anodes for rechargeable lithium batteries," *Solid State Ionics,* vol. 69, no. 3-4, pp. 284-290, 1994.

[23] N. Sato, "Thermal behavior analysis of lithium-ion batteries for electric and hybrid vehicles," *Journal of Power Sources,* vol. 99, no. 1, pp. 70-77, 2001.

[24] A. Eddahech, O. Briat, and J.-M. Vinassa, "Thermal characterization of a high-power lithium-ion battery: Potentiometric and calorimetric measurement of entropy changes," *Energy,* vol. 61, pp. 432-439, 2013.

[25] T. Li, J.-H. Lee, R. Wang, and Y. T. Kang, "Enhancement of heat transfer for thermal energy storage application using stearic acid nanocomposite with multi-walled carbon nanotubes," *Energy,* vol. 55, pp. 752-761, 6/15/ 2013.

[26] C. Y. Jhu, Y. W. Wang, C. M. Shu, J. C. Chang, and H. C. Wu, "Thermal explosion hazards on 18650 lithium ion batteries with a VSP2 adiabatic calorimeter," *J Hazard Mater,* vol. 192, no. 1, pp. 99-107, Aug 15 2011.

[27] Q. Huang, M. Yan, and Z. Jiang, "Thermal study on single electrodes in lithium-ion battery," *Journal of Power Sources,* vol. 156, no. 2, pp. 541-546, 6/1/ 2006.

[28] W. Wu, X. Xiao, and X. Huang, "The effect of battery design parameters on heat generation and utilization in a Li-ion cell," *Electrochimica Acta,* vol. 83, pp. 227-240, 11/30/ 2012.

[29] Y. H. Ye, Y. X. Shi, N. S. Cai, J. Lee, and X. M. He, "Electro-thermal modeling and experimental validation for lithium ion battery," (in English), *Journal of Power Sources,* vol. 199, pp. 227-238, Feb 1 2012.

[30] S. Al Hallaj, J. Prakash, and J. R. Selman, "Characterization of commercial Li-ion batteries using electrochemical–calorimetric measurements," *Journal of Power Sources,* vol. 87, no. 1–2, pp. 186-194, 4// 2000.

[31] R. Srinivasan, "Monitoring dynamic thermal behavior of the carbon anode in a lithium-ion cell using a four-probe technique," *Journal of Power Sources,* vol. 198, pp. 351-358, 1/15/ 2012.

[32] V. V. Viswanathan *et al.*, "Effect of entropy change of lithium intercalation in cathodes and anodes on Li-ion battery thermal management," *Journal of Power Sources,* vol. 195, no. 11, pp. 3720-3729, 2010.

[33] T. Hatchard, D. MacNeil, A. Basu, and J. Dahn, "Thermal model of cylindrical and prismatic lithium-ion cells," *Journal of The Electrochemical Society,* vol. 148, no. 7, pp. A755-A761, 2001.

[34] T. Hatchard, D. MacNeil, D. Stevens, L. Christensen, and J. Dahn, "Importance of Heat Transfer by Radiation in Li-Ion Batteries during Thermal Abuse," *Electrochemical and Solid-State Letters,* vol. 3, no. 7, pp. 305-308, 2000.

[35] R. C. Weast, M. J. Astle, and W. H. Beyer, *CRC handbook of chemistry and physics*. CRC press Boca Raton, FL, 1988.

[36] S. A. Khateeb, S. Amiruddin, M. Farid, J. R. Selman, and S. Al-Hallaj, "Thermal management of Li-ion battery with phase change material for electric scooters: experimental validation," *Journal of Power Sources,* vol. 142, no. 1–2, pp. 345-353, 3/24/ 2005.

[37] S. Al Hallaj and J. R. Selman, "Novel thermal management system for electric vehicle batteries using phase-change material," *Journal of the Electrochemical Society,* Article vol. 147, no. 9, pp. 3231-3236, 2000.

[38] S. A. Khateeb, M. M. Farid, J. R. Selman, and S. Al-Hallaj, "Design and simulation of a lithium-ion battery with a phase change material thermal management system for an electric scooter," *Journal of Power Sources,* vol. 128, no. 2, pp. 292-307, 4/5/ 2004.

[39] S. Al Hallaj, H. Maleki, J. S. Hong, and J. R. Selman, "Thermal modeling and design considerations of lithium-ion batteries," (in English), *Journal of Power Sources,* vol. 83, no. 1-2, pp. 1-8, Oct 1999.

[40] H. Maleki, S. Al Hallaj, J. R. Selman, R. B. Dinwiddie, and H. Wang, "Thermal Properties of Lithium-Ion Battery and Components," *Journal of the Electrochemical Society,* vol. 146, no. 3, pp. 947-954, 1999.

[41] J. S. Hong, H. Maleki, S. Al Hallaj, L. Redey, and J. Selman, "Electrochemical-calorimetric studies of lithium-ion cells," *Journal of the Electrochemical Society,* vol. 145, no. 5, pp. 1489-1501, 1998.

[42] S. Type, "Lithium-ion battery manual," *US18650 Sony Co,* 1993.

[43] C. Forgez, D. V. Do, G. Friedrich, M. Morcrette, and C. Delacourt, "Thermal modeling of a cylindrical LiFePO4/graphite lithium-ion battery," (in English), *Journal of Power Sources,* vol. 195, no. 9, pp. 2961-2968, May 1 2010.

[44] D. H. Jeon and S. M. Baek, "Thermal modeling of cylindrical lithium ion battery during discharge cycle," (in English), *Energy Conversion and Management,* vol. 52, no. 8-9, pp. 2973-2981, Aug 2011.

[45] R. E. Williford, V. V. Viswanathan, and J.-G. Zhang, "Effects of entropy changes in anodes and cathodes on the thermal behavior of lithium ion batteries," *Journal of Power Sources,* vol. 189, no. 1, pp. 101-107, 2009.

[46] U. S. Kim, C. B. Shin, and C.-S. Kim, "Modeling for the scale-up of a lithium-ion polymer battery," *Journal of Power Sources,* vol. 189, no. 1, pp. 841-846, 2009.

[47] Y. Inui, Y. Kobayashi, Y. Watanabe, Y. Watase, and Y. Kitamura, "Simulation of temperature distribution in cylindrical and prismatic lithium ion secondary batteries," *Energy Conversion and Management,* vol. 48, no. 7, pp. 2103-2109, 7// 2007.

[48] G. Sikha, R. E. White, and B. N. Popov, "A mathematical model for a lithium-ion battery/electrochemical capacitor hybrid system," *Journal of the Electrochemical Society,* vol. 152, no. 8, pp. A1682-A1693, 2005.

[49] P. Ramadass, B. Haran, R. White, and B. N. Popov, "Capacity fade of Sony 18650 cells cycled at elevated temperatures: Part I. Cycling performance," *Journal of Power Sources,* vol. 112, no. 2, pp. 606-613, 11/14/ 2002.

[50] D. R. Baker and M. W. Verbrugge, "Temperature and Current Distribution in Thin-Film Batteries," *Journal of the Electrochemical Society,* vol. 146, no. 7, pp. 2413-2424, 1999.

[51] U. S. Kim, C. B. Shin, and C.-S. Kim, "Effect of electrode configuration on the thermal behavior of a lithium-polymer battery," *Journal of Power Sources,* vol. 180, no. 2, pp. 909-916, 2008.

[52] N. Nieto *et al.*, "Thermal modeling of large format lithium-ion cells," *Journal of The Electrochemical Society,* vol. 160, no. 2, pp. A212-A217, 2013.

[53] H.-G. Schweiger *et al.*, "Comparison of Several Methods for Determining the Internal Resistance of Lithium Ion Cells," *Sensors,* vol. 10, no. 6, p. 5604, 2010.

[54] K. Onda, T. Ohshima, M. Nakayama, K. Fukuda, and T. Araki, "Thermal behavior of small lithium-ion battery during rapid charge and discharge cycles," *Journal of Power Sources,* vol. 158, no. 1, pp. 535-542, 7/14/ 2006.

[55] S. Al-Hallaj and J. R. Selman, "Thermal modeling of secondary lithium batteries for electric vehicle/hybrid electric vehicle applications," (in English), *Journal of Power Sources,* vol. 110, no. 2, pp. 341-348, Aug 22 2002.

[56] S. Al Hallaj and J. Selman, "A Novel Thermal Management System for Electric Vehicle Batteries Using Phase-Change Material," *Journal of the Electrochemical Society,* vol. 147, no. 9, pp. 3231-3236, 2000.

[57] C. R. Pals and J. Newman, "Thermal Modeling of the Lithium/Polymer Battery .1. Discharge Behavior of a Single-Cell," (in English), *Journal of the Electrochemical Society,* vol. 142, no. 10, pp. 3274-3281, Oct 1995.

[58] C. R. Pals and J. Newman, "Thermal Modeling of the Lithium/Polymer Battery .2. Temperature Profiles in a Cell Stack," (in English), *Journal of the Electrochemical Society,* vol. 142, no. 10, pp. 3282-3288, Oct 1995.

[59] T. Laher, L. McCurry, and G. Mamantov, "Determination of oxide in aluminium chloride-sodium chloride melts via electrochemical methods," *Analytical chemistry,* vol. 57, no. 2, pp. 500-504, 1985.

[60] J. H. Taylor, W. Benedict, and J. Strong, "Infrared Spectra of H2O and CO2 at 500° C," *The Journal of Chemical Physics,* vol. 20, no. 12, pp. 1884-1898, 1952.

[61] S. Chacko and Y. M. M. Chung, "Thermal modelling of Li-ion polymer battery for electric vehicle drive cycles," (in English), *Journal of Power Sources,* vol. 213, pp. 296-303, Sep 1 2012.

[62] K. Somasundaram, E. Birgersson, and A. S. Mujumdar, "Thermal-electrochemical model for passive thermal management of a spiral-wound lithium-ion battery," (in English), *Journal of Power Sources,* vol. 203, pp. 84-96, Apr 1 2012.

[63] B. A. Johnson and R. E. White, "Characterization of commercially available lithium-ion batteries," *Journal of Power Sources,* vol. 70, no. 1, pp. 48-54, 1998/01/30 1998.

[64] R. Sabbah, R. Kizilel, J. R. Selman, and S. Al-Hallaj, "Active (air-cooled) vs. passive (phase change material) thermal management of high power lithium-ion packs: Limitation of temperature rise and uniformity of temperature distribution," *Journal of Power Sources,* vol. 182, no. 2, pp. 630-638, 8/1/ 2008.

[65] A. Mills and S. Al-Hallaj, "Simulation of passive thermal management system for lithium-ion battery packs," *Journal of Power Sources,* vol. 141, no. 2, pp. 307-315, 3/1/ 2005.

[66] R. Kizilel, R. Sabbah, J. R. Selman, and S. Al-Hallaj, "An alternative cooling system to enhance the safety of Li-ion battery packs," *Journal of Power Sources,* vol. 194, no. 2, pp. 1105-1112, 12/1/ 2009.

[67] P. Taheri, M. Yazdanpour, and M. Bahrami, "Transient three-dimensional thermal model for batteries with thin electrodes," (in English), *Journal of Power Sources,* vol. 243, pp. 280-289, Dec 1 2013.

[68] J. Newman and W. Tiedemann, "Temperature rise in a battery module with constant heat generation," *Journal of the Electrochemical Society,* vol. 142, no. 4, pp. 1054-1057, 1995.

[69] M. N. Özışık, *Boundary value problems of heat conduction*. Courier Corporation, 1989.

[70] J. Lee, K. Choi, N. Yao, and C. Christianson, "Three-Dimensional Thermal Modeling of Electric Vehicle Batteries," *Journal of The Electrochemical Society,* vol. 133, no. 7, pp. 1286-1291, 1986.

[71] Y. Chen and J. W. Evans, "Three-Dimensional Thermal Modeling of Lithium-Polymer Batteries under Galvanostatic Discharge and Dynamic Power Profile," *Journal of the Electrochemical Society,* vol. 141, no. 11, pp. 2947-2955, 1994.

[72] D. H. Jeon, "Numerical modeling of lithium ion battery for predicting thermal behavior in a cylindrical cell," (in English), *Current Applied Physics,* vol. 14, no. 2, pp. 196-205, Feb 2014.

[73] P. Ramadass, B. Haran, R. White, and B. N. Popov, "Mathematical modeling of the capacity fade of Li-ion cells," *Journal of Power Sources,* vol. 123, no. 2, pp. 230-240, 9/20/ 2003.

[74] P. Ramadass, B. Haran, P. M. Gomadam, R. White, and B. N. Popov, "Development of first principles capacity fade model for Li-ion cells," *Journal of the Electrochemical Society,* vol. 151, no. 2, pp. A196-A203, 2004.

[75] S. Santhanagopalan, Q. Guo, P. Ramadass, and R. E. White, "Review of models for predicting the cycling performance of lithium ion batteries," *Journal of Power Sources,* vol. 156, no. 2, pp. 620-628, 6/1/ 2006.

[76] S. Santhanagopalan, Q. Guo, and R. E. White, "Parameter estimation and model discrimination for a lithium-ion cell," *Journal of the Electrochemical Society,* vol. 154, no. 3, pp. A198-A206, 2007.

[77] J. Marcicki and X. G. Yang, "Model-Based Estimation of Reversible Heat Generation in Lithium-Ion Cells," *Journal of The Electrochemical Society,* vol. 161, no. 12, pp. A1794-A1800, 2014.

[78] L. Rao and J. Newman, "Heat-Generation Rate and General Energy Balance for Insertion Battery Systems," *Journal of the Electrochemical Society,* vol. 144, no. 8, pp. 2697-2704, 1997.

[79] K. E. Thomas and J. Newman, "Heats of mixing and of entropy in porous insertion electrodes," *Journal of power sources,* vol. 119, pp. 844-849, 2003.

[80] S. Drake *et al.*, "Heat generation rate measurement in a Li-ion cell at large C-rates through temperature and heat flux measurements," *Journal of Power Sources,* vol. 285, pp. 266-273, 2015.

[81] K. Shah *et al.*, "An experimentally validated transient thermal model for cylindrical Li-ion cells," *Journal of Power Sources,* vol. 271, pp. 262-268, 2014.

[82] L. Saw, Y. Ye, and A. Tay, "Electrochemical–thermal analysis of 18650 lithium iron phosphate cell," *Energy Conversion and Management,* vol. 75, pp. 162-174, 2013.

[83] S. Zhang, K. Xu, and T. Jow, "Charge and discharge characteristics of a commercial LiCoO 2-based 18650 Li-ion battery," *Journal of Power Sources,* vol. 160, no. 2, pp. 1403-1409, 2006.

[84] D. Ragone, "Mid-Year Meeting of the Society of Automotive Engineers," *Detroit, MI, May,* pp. 20-24, 1968.

[85] V. Srinivasan and C. Wang, "Analysis of electrochemical and thermal behavior of Li-ion cells," *Journal of The Electrochemical Society,* vol. 150, no. 1, pp. A98-A106, 2003.

[86] G.-H. Kim, A. Pesaran, and R. Spotnitz, "A three-dimensional thermal abuse model for lithium-ion cells," *Journal of Power Sources,* vol. 170, no. 2, pp. 476-489, 2007.

[87] A. A. Pesaran, "Battery thermal management in EV and HEVs: issues and solutions," *Battery Man,* vol. 43, no. 5, pp. 34-49, 2001.

[88] T. Wang, K. Tseng, J. Zhao, and Z. Wei, "Thermal investigation of lithium-ion battery module with different cell arrangement structures and forced air-cooling strategies," *Applied Energy,* vol. 134, pp. 229-238, 2014.

[89] S. Basu, K. S. Hariharan, S. M. Kolake, T. Song, D. K. Sohn, and T. Yeo, "Coupled electrochemical thermal modelling of a novel Li-ion battery pack thermal management system," *Applied Energy,* vol. 181, pp. 1-13, 2016.

[90] H. G. Sun, X. H. Wang, B. Tossan, and R. Dixon, "Three-dimensional thermal modeling of a lithium-ion battery pack," (in English), *Journal of Power Sources,* vol. 206, pp. 349-356, May 15 2012.

[91] L. Fan, J. Khodadadi, and A. Pesaran, "A parametric study on thermal management of an air-cooled lithium-ion battery module for plug-in hybrid electric vehicles," *Journal of Power Sources,* vol. 238, pp. 301-312, 2013.

[92] M. Guo and R. E. White, "Mathematical model for a spirally-wound lithium-ion cell," *Journal of Power Sources,* vol. 250, pp. 220-235, 2014.

[93] R. Zhao, S. Zhang, J. Gu, J. Liu, S. Carkner, and E. Lanoue, "An experimental study of lithium ion battery thermal management using flexible hydrogel films," *Journal of Power Sources,* vol. 255, pp. 29-36, 2014.

[94] J. Zhao, Z. Rao, Y. Huo, X. Liu, and Y. Li, "Thermal management of cylindrical power battery module for extending the life of new energy electric vehicles," *Applied Thermal Engineering,* vol. 85, pp. 33-43, 2015.

[95] F. He and L. Ma, "Thermal Management in Hybrid Power Systems Using Cylindrical and Prismatic Battery Cells," *Heat Transfer Engineering,* vol. 37, no. 6, pp. 581-590, 2016.

[96] L. Song *et al.,* "Estimation of temperature distribution of LiFePO4 lithium ion battery during charge–discharge process," *Ionics,* pp. 1-9, 2016.

[97] Z. H. C. Daud, D. Chrenko, F. Dos Santos, E. Aglzim, A. Keromnes, and L. Le Moyne, "3D electro-thermal modelling and experimental validation of lithium polymer-based batteries for automotive applications," (in English), *International Journal of Energy Research,* vol. 40, no. 8, pp. 1144-1154, Jun 25 2016.

[98] Azosensors. (03/02). *ES-Accelerating Rate Calorimeter from Thermal Hazard Technology*. Available: http://www.azosensors.com/equipment-details.aspx?EquipID=84

[99] G. Zhang, L. Cao, S. Ge, C.-Y. Wang, C. E. Shaffer, and C. D. Rahn, "In situ measurement of radial temperature distributions in cylindrical li-ion cells," *Journal of The Electrochemical Society,* vol. 161, no. 10, pp. A1499-A1507, 2014.

[100] Y. Ji, Y. Zhang, and C.-Y. Wang, "Li-ion cell operation at low temperatures," *Journal of The Electrochemical Society,* vol. 160, no. 4, pp. A636-A649, 2013.